

# Reduced density matrices and coherence of trapped interacting bosons

Kaspar Sakmann\*, Alexej I. Streltsov†, Ofir E. Alon‡, and Lorenz S. Cederbaum§

*Theoretische Chemie, Universität Heidelberg, D-69120 Heidelberg, Germany*

## Abstract

The first- and second-order correlation functions of trapped, interacting Bose-Einstein condensates are investigated numerically on a many-body level from first principles. Correlations in real space and momentum space are treated. The coherence properties are analyzed. The results are obtained by solving the many-body Schrödinger equation. It is shown in an example how many-body effects can be induced by the trap geometry. A generic fragmentation scenario of a condensate is considered. The correlation functions are discussed along a pathway from a single condensate to a fragmented condensate. It is shown that strong correlations can arise from the geometry of the trap, even at weak interaction strengths. The natural orbitals and natural geminals of the system are obtained and discussed. It is shown how the fragmentation of the condensate can be understood in terms of its natural geminals. The many-body results are compared to those of mean-field theory. The best solution within mean-field theory is obtained. The limits in which mean-field theories are valid are determined. In these limits the behavior of the correlation functions is explained within an analytical model.

PACS numbers: 05.30.Jp, 03.65.-w, 03.75.Hh, 03.75.Nt

---

\* Corresponding author, E-mail: kaspar.sakmann@pci.uni-heidelberg.de

† E-mail: alexej.streltsov@pci.uni-heidelberg.de

‡ E-mail: ofir.alon@pci.uni-heidelberg.de

§ E-mail: lorenz.cederbaum@pci.uni-heidelberg.de

## I. INTRODUCTION

The computation of correlation functions in interacting quantum many-body systems is a challenging problem of contemporary physics. Correlations between particles can exist in time, in real space or in momentum space. Of course, all combinations of the above three cases are possible. Since the first experimental realization of Bose-Einstein condensates (BECs) in ultracold atomic gases [1–3], great experimental and theoretical progress has been made in the determination of the coherence and the correlation functions of Bose-condensed systems. Over the years experiments have measured more and more accurately first, second and to some extent even third order correlations of trapped BECs, see [4–11]. Theoretically, the correlation functions of trapped, interacting BECs have been investigated in numerous works, see e.g. [12–21]. While analytical approaches from first principles are usually restricted to treat homogeneous gases without any trapping potential, numerical methods can overcome this restriction. It is important to note that the shape of the trapping potential can have a substantial impact on the properties of the many-body system. This is particularly true for issues concerning condensation [22] and fragmentation of Bose systems [23]. For example, the ground state of weakly interacting condensates in harmonic traps is almost fully condensed, while the ground state of double-well potentials can be fragmented or condensed, depending on the height of the barrier, the number of particles and the interaction strength [24–29]. In this work we investigate first- and second-order correlations of trapped, interacting condensates and their coherence properties depending on the trap geometry from first principles. Our results are obtained by solving the many-body Schrödinger equation of the interacting system numerically. From this many-body solution we extract the first- and second-order reduced density matrices which allow us to compute all real and momentum space first- and second-order correlations and in particular the fragmentation of the condensate. For illustration purposes we consider a stationary system in the ground state to show how many-body effects can become dominant when the trap geometry is varied. As a numerical method to solve the interacting many-body problem we use the recently developed *multiconfigurational time-dependent Hartree for bosons* (MCTDHB), which propagates a given many-body state in time [30–32]. By propagation in imaginary time it allows us to investigate the ground state and other stationary states. Alternatively, one can use the stationary multiconfigurational Hartree for bosons to compute these states

[29]. In order to identify true many-body effects in the correlation functions, we compare our many-body results with those based on mean-field approaches. More specifically, we compute the energetically-lowest mean-field solution of the same system for comparison. This is the best approximation to the true many-body wave-function within mean-field theory and, thereby, allows us to pinpoint the limits of mean-field theory. A general method to compute this *best mean-field* solution has been developed in our group [25–28, 33]. For completeness we compare the many-body results also to the widely used Gross-Pitaevskii mean-field solution. In order to understand first- and second-order correlations in an intuitive way, we develop an analytical mean-field model which explains the general structure of our results in those regions where many-body effects can be safely neglected.

This paper is organized as follows. In Sec. II we review basic facts about reduced density matrices, correlation functions and coherence. In Sec. III we give a brief introduction to the numerical many-body and mean-field methods that we use. In Sec. IV we introduce a generic one-dimensional model system that we solve. In particular, we identify mean-field and many-body regimes of this system. We explain the transition from a condensed to a fragmented state in terms of the natural geminals of the system. In Secs. V and VI we present our many-body results for the first- and second-order correlation functions and the coherence properties of the model system. We compare our many-body results with those obtained by using the *best mean-field* and the Gross-Pitaevskii approximation. The structure of the correlation functions and the coherence are explained within an analytical mean-field model in the limits where mean-field theory is applicable.

## II. BASIC DEFINITIONS

We consider a given wave function  $\Psi(\mathbf{r}_1, \dots, \mathbf{r}_N; t)$  of  $N$  identical, spinless bosons with spatial coordinates  $\mathbf{r}_i$  in  $D$  dimensions. The  $p$ -th order reduced density matrix (RDM), is defined by

$$\begin{aligned} \rho^{(p)}(\mathbf{r}_1, \dots, \mathbf{r}_p | \mathbf{r}'_1, \dots, \mathbf{r}'_p; t) = & \frac{N!}{(N-p)!} \int \Psi(\mathbf{r}_1, \dots, \mathbf{r}_p, \mathbf{r}_{p+1}, \dots, \mathbf{r}_N; t) \\ & \times \Psi^*(\mathbf{r}'_1, \dots, \mathbf{r}'_p, \mathbf{r}_{p+1}, \dots, \mathbf{r}_N; t) d\mathbf{r}_{p+1} \dots d\mathbf{r}_N, \end{aligned} \quad (1)$$

where the wave function is assumed to be normalized  $\langle \Psi(t) | \Psi(t) \rangle = 1$ . Equivalent to Eq. (1),  $\rho^{(p)}(\mathbf{r}_1, \dots, \mathbf{r}_p | \mathbf{r}'_1, \dots, \mathbf{r}'_p; t)$  can be regarded as the kernel of the operator

$$\hat{\rho}^{(p)} = \frac{N!}{(N-p)!} \text{Tr}_{N-p} [|\Psi(t)\rangle \langle \Psi(t)|] \quad (2)$$

in Hilbert space, where  $\text{Tr}_{N-p}[\cdot]$  specifies taking the partial trace over  $N-p$  particles. Since the wave function is symmetric in its coordinates, it does not matter over which particles the trace is taken. In what follows, we add  $|\Psi\rangle$  as an additional subscript if a result is only valid for states  $|\Psi\rangle$  of a particular form.

The diagonal  $\rho^{(p)}(\mathbf{r}_1, \dots, \mathbf{r}_p | \mathbf{r}_1, \dots, \mathbf{r}_p; t)$  is the  $p$ -particle probability distribution at time  $t$  multiplied by  $N!/(N-p)!$ . The  $p$ -th order RDM  $\rho^{(p)}$  can be expanded in its eigenfunctions, leading to the representation

$$\rho^{(p)}(\mathbf{r}_1, \dots, \mathbf{r}_p | \mathbf{r}'_1, \dots, \mathbf{r}'_p; t) = \sum_i n_i^{(p)}(t) \alpha_i^{(p)}(\mathbf{r}_1, \dots, \mathbf{r}_p, t) \alpha_i^{(p)*}(\mathbf{r}'_1, \dots, \mathbf{r}'_p, t). \quad (3)$$

Here,  $n_i^{(p)}(t)$  denotes the  $i$ -th eigenvalue of the  $p$ -th order RDM and  $\alpha_i^{(p)}(\mathbf{r}_1, \dots, \mathbf{r}_p, t)$  the corresponding eigenfunction. The eigenfunctions are known as *natural  $p$ -functions* and the eigenvalues as *natural occupations*. For  $p=1$  and  $p=2$  the eigenfunctions are also known as *natural orbitals* and *natural geminals*, respectively. We order the eigenvalues  $n_i^{(p)}(t)$  for every  $p$  non-increasingly, such that  $n_1^{(p)}(t)$  denotes the largest eigenvalue of the  $p$ -th order RDM. The normalization of the many-body wave function and Eqs. (1) and (3) put the restriction

$$\sum_i n_i^{(p)}(t) = \frac{N!}{(N-p)!} \quad (4)$$

on the eigenvalues of the  $p$ -th order RDM. Thus the largest eigenvalue  $n_1^{(p)}(t)$  is bounded from above by [34, 35]

$$n_1^{(p)}(t) \leq \frac{N!}{(N-p)!}. \quad (5)$$

Lower bounds on  $n_1^{(p)}(t)$  can be derived, relating RDMs of different order [36, 37]. In particular, for the case  $p=2$  it can be shown that [36]

$$n_1^{(2)}(t) \geq n_1^{(1)}(t)[n_1^{(1)}(t) - 1]. \quad (6)$$

It is a well known fact that the natural orbitals of a symmetric (or antisymmetric) function  $\Psi$  constitute a sufficient one-particle basis to expand  $\Psi$  and the eigenfunctions of the RDMs

for all  $p$  [34]. It is therefore possible to construct the natural geminals in the basis of one-particle functions spanned by the natural orbitals.

The determination of accurate bounds on eigenvalues of RDMs is an active field of research [34, 35] since it is possible to express the *exact* energy expectation value of a quantum system of identical particles interacting via two-body interactions by an expression involving only the natural geminals,  $\alpha_i^{(2)}(\mathbf{r}_1, \mathbf{r}_2, t)$ , and their occupations,  $n_i^{(2)}(t)$ . For a general Hamiltonian

$$H = \sum_{i=1}^N h(\mathbf{r}_i) + \sum_{i<j}^N W(\mathbf{r}_i - \mathbf{r}_j), \quad (7)$$

consisting of one-body operators  $h(\mathbf{r}_i)$  and two-body operators  $W(\mathbf{r}_i - \mathbf{r}_j)$ , the expectation value of the energy  $E$  can be expressed by making use of the time-dependent natural geminals  $\alpha_i^{(2)}(x_1, x_2, t)$  and following Refs. [34, 35] through the equation:

$$E = \frac{1}{2} \sum_i n_i^{(2)}(t) \int d\mathbf{r}_1 d\mathbf{r}_2 \alpha_i^{(2)*}(\mathbf{r}_1, \mathbf{r}_2, t) \left[ \frac{h(\mathbf{r}_1) + h(\mathbf{r}_2)}{N-1} + W(\mathbf{r}_1 - \mathbf{r}_2) \right] \alpha_i^{(2)}(\mathbf{r}_1, \mathbf{r}_2, t). \quad (8)$$

Note that the many-body wave function does not appear explicitly in Eq. (8). We will not go any further into the details of these approaches to many-body physics and refer the reader to the literature [34, 35].

The natural orbitals also serve to define Bose-Einstein condensation in interacting systems. According to Penrose and Onsager [22], a system of identical bosons is said to be *condensed*, if the largest eigenvalue of the first-order RDM is of the order of the number of particles in the system,  $n_1^{(1)} = \mathcal{O}(N)$ . If more than one eigenvalue of the first-order RDM is of the order of the number of particles, the condensate is said to be *fragmented*, according to Nozières and Saint James [23].

Equivalent to Eq. (1), the  $p$ -th order RDM can be expressed through field operators as

$$\rho^{(p)}(\mathbf{r}_1, \dots, \mathbf{r}_p | \mathbf{r}'_1, \dots, \mathbf{r}'_p; t) = \langle \Psi(t) | \hat{\Psi}^\dagger(\mathbf{r}'_1) \dots \hat{\Psi}^\dagger(\mathbf{r}'_p) \hat{\Psi}(\mathbf{r}_p) \dots \hat{\Psi}(\mathbf{r}_1) | \Psi(t) \rangle, \quad (9)$$

where the Schrödinger field operators satisfy the usual bosonic commutation relations

$$\left[ \hat{\Psi}(\mathbf{r}), \hat{\Psi}^\dagger(\mathbf{r}') \right] = \delta(\mathbf{r} - \mathbf{r}'), \quad \left[ \hat{\Psi}(\mathbf{r}), \hat{\Psi}(\mathbf{r}') \right] = 0. \quad (10)$$

The representation given in Eq. (9) shows that the  $p$ -th order RDM is identical to the  $p$ -th order correlation function at equal times [12, 38].

In order to discuss correlations not only in real space, but also in momentum space, we define the Fourier transform of a function  $f(\mathbf{r}_1, \dots, \mathbf{r}_p)$  of  $p$   $D$ -dimensional coordinates  $\mathbf{r}_i$  by

$$f(\mathbf{k}_1, \dots, \mathbf{k}_p) = \frac{1}{(2\pi)^{pD/2}} \int d^p \mathbf{r} e^{-i \sum_{i=1}^p \mathbf{k}_i \mathbf{r}_i} f(\mathbf{r}_1, \dots, \mathbf{r}_p). \quad (11)$$

By applying the Fourier transform, Eq. (11), to the coordinates  $\mathbf{r}_1, \dots, \mathbf{r}_p$  and  $\mathbf{r}'_1, \dots, \mathbf{r}'_p$  of the natural  $p$ -functions  $\alpha_i^{(p)}(\mathbf{r}_1, \dots, \mathbf{r}_p, t)$  and  $\alpha_i^{(p)}(\mathbf{r}'_1, \dots, \mathbf{r}'_p, t)$  in Eq. (3), one arrives at the momentum space representation of  $\hat{\rho}^{(p)}$ :

$$\rho^{(p)}(\mathbf{k}_1, \dots, \mathbf{k}_p | \mathbf{k}'_1, \dots, \mathbf{k}'_p; t) = \sum_i n_i^{(p)}(t) \alpha_i^{(p)}(\mathbf{k}_1, \dots, \mathbf{k}_p, t) \alpha_i^{(p)*}(\mathbf{k}'_1, \dots, \mathbf{k}'_p, t). \quad (12)$$

The diagonal  $\rho^{(p)}(\mathbf{k}_1, \dots, \mathbf{k}_p | \mathbf{k}_1, \dots, \mathbf{k}_p; t)$  in momentum space is the  $p$ -particle momentum distribution at time  $t$ , multiplied by  $N!/(N-p)!$ . It can be shown that the  $p$ -particle momentum distribution at large momenta is dominated by contributions of  $\rho^{(p)}(\mathbf{r}_1, \dots, \mathbf{r}_p | \mathbf{r}'_1, \dots, \mathbf{r}'_p; t)$  close to the diagonal, i.e.  $\mathbf{r}_i \approx \mathbf{r}'_i$  for  $i = 1, \dots, p$ . Similarly, the  $p$ -particle distribution at low momenta is dominated by the behavior of  $\rho^{(p)}(\mathbf{r}_1, \dots, \mathbf{r}_p | \mathbf{r}'_1, \dots, \mathbf{r}'_p; t)$  on the off-diagonal at large distances between  $\mathbf{r}_i$  and  $\mathbf{r}'_i$ . See Appendix A for more details.

Apart from the  $p$ -particle distributions themselves, either in real space or in momentum space, it is also of great interest to compare the  $p$ -particle probabilities to their respective one-particle probabilities. Thereby, it becomes possible to identify effects that are due to the quantum statistics of the particles. The *normalized  $p$ -th order correlation function* at time  $t$  is defined by [38]

$$g^{(p)}(\mathbf{r}'_1, \dots, \mathbf{r}'_p, \mathbf{r}_1, \dots, \mathbf{r}_p; t) = \frac{\rho^{(p)}(\mathbf{r}_1, \dots, \mathbf{r}_p | \mathbf{r}'_1, \dots, \mathbf{r}'_p; t)}{\sqrt{\prod_{i=1}^p \rho^{(1)}(\mathbf{r}_i | \mathbf{r}_i; t) \rho^{(1)}(\mathbf{r}'_i | \mathbf{r}'_i; t)}} \quad (13)$$

and is the key quantity in the definition of spatial coherence. Full spatial  $p$ -th order coherence is obtained if  $\rho^{(n)}(\mathbf{r}_1, \dots, \mathbf{r}_p | \mathbf{r}'_1, \dots, \mathbf{r}'_p; t)$  factorizes for all  $n \leq p$  into a product of *one* complex valued function  $\mathcal{E}(\mathbf{r}, t)$  of the form

$$\rho^{(n)}(\mathbf{r}_1, \dots, \mathbf{r}_p | \mathbf{r}'_1, \dots, \mathbf{r}'_p; t) = \mathcal{E}^*(\mathbf{r}'_1, t) \cdots \mathcal{E}^*(\mathbf{r}'_n, t) \mathcal{E}(\mathbf{r}_n, t) \cdots \mathcal{E}(\mathbf{r}_1, t). \quad (14)$$

In this case

$$|g^{(n)}(\mathbf{r}'_1, \dots, \mathbf{r}'_p, \mathbf{r}_1, \dots, \mathbf{r}_p; t)| = 1 \quad (15)$$

for all  $n \leq p$ . Otherwise, the state  $|\Psi(t)\rangle$  is only partially coherent. Full coherence in a system with a definite number of particles  $N$  can only be obtained for  $p = 1$  [39]. However,

when the particle number  $N$  is large,  $p$ -th order coherence can be obtained up to corrections  $\mathcal{O}(1/N)$ , at least for  $p \ll N$  [39].

The diagonal of the normalized  $p$ -th order correlation function  $g^{(p)}(\mathbf{r}_1, \dots, \mathbf{r}_p, \mathbf{r}_1, \dots, \mathbf{r}_p; t)$  gives a measure for the degree of  $p$ -th order coherence. For values  $g^{(p)}(\mathbf{r}_1, \dots, \mathbf{r}_p, \mathbf{r}_1, \dots, \mathbf{r}_p; t) > 1$  ( $< 1$ ) the detection probabilities at positions  $\mathbf{r}_1, \dots, \mathbf{r}_p$  are correlated (anticorrelated).

Note that if Eq. (14) holds in real space, it must also hold in momentum space, as can be seen by Fourier transforming each of the  $2n$  variables in Eq. (14). It is therefore possible to define the normalized  $p$ -th order correlation function in momentum space by

$$g^{(p)}(\mathbf{k}'_1, \dots, \mathbf{k}'_p, \mathbf{k}_1, \dots, \mathbf{k}_p; t) = \frac{\rho^{(p)}(\mathbf{k}_1, \dots, \mathbf{k}_p | \mathbf{k}'_1, \dots, \mathbf{k}'_p; t)}{\sqrt{\prod_{i=1}^p \rho^{(1)}(\mathbf{k}_i | \mathbf{k}_i; t) \rho^{(1)}(\mathbf{k}'_i | \mathbf{k}'_i; t)}}. \quad (16)$$

The diagonal of Eq. (16),  $g^{(p)}(\mathbf{k}_1, \dots, \mathbf{k}_p, \mathbf{k}_1, \dots, \mathbf{k}_p; t)$ , expresses the tendency of  $p$  momenta to be measured simultaneously. For values  $g^{(p)}(\mathbf{k}_1, \dots, \mathbf{k}_p, \mathbf{k}_1, \dots, \mathbf{k}_p; t) > 1$  ( $< 1$ ) the detection probabilities of momenta  $\mathbf{k}_1, \dots, \mathbf{k}_p$  are correlated (anticorrelated). The  $p$ -th order momentum distribution  $\rho^{(p)}(\mathbf{k}_1, \dots, \mathbf{k}_p | \mathbf{k}_1, \dots, \mathbf{k}_p; t)$  depends on the entire  $p$ -th order RDM  $\rho^{(p)}(\mathbf{r}_1, \dots, \mathbf{r}_p | \mathbf{r}'_1, \dots, \mathbf{r}'_p; t)$ , see Appendix A. Thus,  $g^{(p)}(\mathbf{k}_1, \dots, \mathbf{k}_p, \mathbf{k}_1, \dots, \mathbf{k}_p; t)$  provides information about the coherence of  $|\Psi(t)\rangle$  which is not contained in  $g^{(p)}(\mathbf{r}_1, \dots, \mathbf{r}_p, \mathbf{r}_1, \dots, \mathbf{r}_p; t)$ .

In Young double slit experiments using non-interacting bosons  $|g^{(1)}(\mathbf{r}'_1, \mathbf{r}_1; t_0)| = 1$  ensures the maximal fringe visibility of an interference pattern. Here,  $t_0$  is the time of release from the slits. See, e.g. [40], for an experiment using Bose-Einstein condensates. However, if interactions during the expansion behind the slit are not negligible, there is no simple relation between the fringe visibility and the wave function  $\Psi(\mathbf{r}_1, \dots, \mathbf{r}_N, t_0)$  at the time of release from the slits. In other words, the interaction between the particles can modify the observed interference pattern [41–43].

In order to determine the degree of coherence of a given system, it is necessary to quantify how well Eq. (14) is satisfied. A visualization of the degree of coherence is highly desirable, as it helps to understand the coherence limiting factors in an intuitive manner. Already for one-dimensional systems,  $D = 1$ , the normalized first-order correlation function at time  $t$ ,  $g^{(1)}(\mathbf{r}'_1, \mathbf{r}_1; t)$ , is a complex function of two variables and cannot be visualized in a single plot. It is, therefore, necessary to consider quantities that sample parts of  $g^{(p)}(\mathbf{r}'_1, \dots, \mathbf{r}'_p, \mathbf{r}_1, \dots, \mathbf{r}_p; t)$ . In one-dimensional systems  $|g^{(1)}(\mathbf{r}'_1, \mathbf{r}_1; t)|^2$  can be represented as a two-dimensional plot and gives a measure for the degree of first-order coher-

ence. Similarly,  $g^{(2)}(\mathbf{r}_1, \mathbf{r}_2, \mathbf{r}_1, \mathbf{r}_2; t)$  and  $g^{(2)}(\mathbf{k}_1, \mathbf{k}_2, \mathbf{k}_1, \mathbf{k}_2; t)$  are real and can be represented as two-dimensional plots, if  $D = 1$ . In Secs. V and VI we will visualize the degree of first- and second-order coherence of a one-dimensional system, defined in Sec. IV, by means of  $|g^{(1)}(\mathbf{r}'_1, \mathbf{r}_1; t)|^2$ ,  $g^{(2)}(\mathbf{r}_1, \mathbf{r}_2, \mathbf{r}_1, \mathbf{r}_2; t)$  and  $g^{(2)}(\mathbf{k}_1, \mathbf{k}_2, \mathbf{k}_1, \mathbf{k}_2; t)$ .

### III. NUMERICAL METHODS

The main goal of this work is to investigate exactly the behavior of first- and second-order correlation functions in interacting many-body systems. This requires the computation of the exact many-body wave function which is generally a difficult problem to solve. In some cases, when the general form of the wave function is known *a priori*, an exact solution can be obtained, either by solving transcendental equations or by exploiting mapping theorems, see e.g. [18, 44–52]. However, in general it is necessary to solve the full many-body Schrödinger equation numerically in an efficient way. In Sec. III A we give a brief account of the numerical method MCTDHB to solve the interacting many-boson problem. In order to find out to which extent mean-field methods are applicable to bosonic, interacting many-body systems, we compare our many-body results with those based on mean-field approaches, namely the commonly used Gross-Pitaevskii mean-field [53–55] and the *best mean-field* (BMF), which we describe briefly in Sec. III B. It is beyond the scope of this work to explain either MCTDHB or BMF in detail and we refer the reader to Refs. [30–32] and Refs. [25–28, 33] for more detailed explanations of MCTDHB and BMF, respectively.

#### A. The many-body wave function

The exact wave function of an interacting  $N$ -boson problem can always be expanded in any complete set of permanents of  $N$  particles. Each of the permanents is constructed from a complete set of single-particle functions which are commonly referred to as *orbitals*. Practical computations can *never* be carried out in complete basis sets and therefore, it is crucial to cut the basis set carefully.

Our starting point is the Schrödinger picture field operator  $\hat{\Psi}(\mathbf{r})$  satisfying the usual bosonic commutation relations Eqs. (10). It is convenient to expand the field operator in a



complete set of *time-dependent* orthonormal orbitals,

$$\hat{\Psi}(\mathbf{r}) = \sum_k \hat{c}_k(t) \phi_k(\mathbf{r}, t), \quad (17)$$

where the time-dependent annihilation and creation operators obey the usual commutation relations  $\hat{c}_k(t) \hat{c}_j^\dagger(t) - \hat{c}_j^\dagger(t) \hat{c}_k(t) = \delta_{kj}$  for bosons at any time. Note that it is not necessary to specify the shape of the orbitals at this point.

The many-body Hamiltonian (7) is standardly written in second quantized form as

$$\hat{H} = \sum_{k,q} \hat{c}_k^\dagger \hat{c}_q h_{kq} + \frac{1}{2} \sum_{k,s,l,q} \hat{c}_k^\dagger \hat{c}_s^\dagger \hat{c}_l \hat{c}_q W_{ksql}, \quad (18)$$

where the matrix elements of the one-body Hamiltonian  $h(\mathbf{r})$  and two-body interaction potential  $W(\mathbf{r} - \mathbf{r}')$  are given by

$$\begin{aligned} h_{kq}(t) &= \int \phi_k^*(\mathbf{r}, t) h(\mathbf{r}) \phi_q(\mathbf{r}, t) d\mathbf{r}, \\ W_{ksql}(t) &= \iint \phi_k^*(\mathbf{r}, t) \phi_s^*(\mathbf{r}', t) W(\mathbf{r} - \mathbf{r}') \phi_q(\mathbf{r}, t) \phi_l(\mathbf{r}', t) d\mathbf{r} d\mathbf{r}'. \end{aligned} \quad (19)$$

The *ansatz* for the many-body wave function  $|\Psi(t)\rangle$  in MCTDHB is taken as a linear combination of time-dependent permanents

$$\begin{aligned} |\Psi(t)\rangle &= \sum_{\vec{n}} C_{\vec{n}}(t) |n_1, n_2, \dots, n_M; t\rangle, \\ |n_1, n_2, \dots, n_M; t\rangle &= \frac{1}{\sqrt{n_1! n_2! \dots n_M!}} \left( \hat{c}_1^\dagger(t) \right)^{n_1} \left( \hat{c}_2^\dagger(t) \right)^{n_2} \dots \left( \hat{c}_M^\dagger(t) \right)^{n_M} |vac\rangle, \end{aligned} \quad (20)$$

where  $|n_1, n_2, \dots, n_M; t\rangle$  is assembled from the time-dependent orbitals above. The summation in (20) runs over all  $\binom{N+M-1}{N}$  permanents generated by distributing  $N$  bosons over  $M$  orbitals. We collect the occupations in the vector  $\vec{n} = (n_1, n_2, \dots, n_M)$ , where  $n_1 + n_2 + \dots + n_M = N$ . Of course, if  $M$  goes to infinity then the *ansatz* (20) for the wave function becomes exact since the set of permanents  $|n_1, n_2, \dots, n_M; t\rangle$  spans the complete  $N$ -particle Hilbert space. In practical computations we have to restrict the number  $M$  of orbitals from which the permanents  $|n_1, n_2, \dots, n_M; t\rangle$  are assembled. By substituting the many-body *ansatz* (20) into the action functional of the time-dependent Schrödinger equation, it is possible to derive a coupled set of equations of motion containing the coefficients  $C_{\vec{n}}(t)$  and the set of time-dependent orbitals  $\phi_k(\mathbf{r}, t)$ . The equations are obtained by requiring the stationarity of the action functional with respect to variations of the coefficients

$C_{\vec{n}}(t)$  and the set of time-dependent orbitals  $\phi_k(\mathbf{r}, t)$ . These coupled equations have to be solved simultaneously, leading to an efficient wave package propagation method for bosons [30–32]. At first sight it might seem to be an unnecessary complication to allow the orbitals  $\phi_k(\mathbf{r}, t)$  to depend on time. However, this additional degree of freedom allows both, the basis of one-particle functions  $\phi_k(\mathbf{r}, t)$  and the coefficients  $C_{\vec{n}}(t)$  to be variationally optimal at any time. Note that this is fundamentally different to a multi-mode *ansatz* with fixed orbitals in which the quality of the chosen basis set may deteriorate as the system evolves in time.

In order to investigate stationary properties of Bose-Einstein condensates, we use a many-body relaxation method. By propagating a given initial guess in imaginary time with MCTDHB, the system relaxes to the ground state, which allows us to treat stationary systems as well. A necessary requirement for this procedure to work is that the initial guess has non-zero overlap with the ground state. The variational principle ensures that the set of orbitals  $\phi_k$  is variationally optimal, in the sense that the lowest ground state energy within the Hilbert subspace of  $N$  bosons distributed over  $M$  orbitals is obtained, see in this respect Ref. [29]. We will not go any further into the details of MCTDHB and refer the reader to the literature [30–32].

## B. Best mean-field

The exact many-body wave function of a bosonic system of  $N$  particles can always be expanded in an infinite weighted sum over any complete set of permanents of  $N$  particles. In mean-field theory the exact many-body wave function is approximated by a single permanent. This single permanent is built from a number  $M \leq N$  of orthogonal orbitals in which the  $N$  bosons reside. In the field of Bose-Einstein condensates one particular mean-field, the Gross-Pitaevskii (GP) mean-field, has proven to be very successful. In analogy to non-interacting BECs, in GP theory it is assumed that the many-body wave function is given by a single permanent in which all particles reside in *one* orbital, i.e.  $M = 1$ . A minimization of the energy functional with the GP *ansatz* wave function leads to the famous Gross-Pitaevskii equation [53–55]. The solution of the GP equation yields the single orbital from which the GP mean-field permanent is constructed.

However, it has been shown [25–28, 33] that the GP mean-field is not always the energetically-lowest mean-field solution. The assumption that *all* particles occupy the same

orbital is too restrictive. Especially in multi-well trapping geometries the energetically-lowest mean-field solution can be fragmented [25–28, 33], see also Sec. II.

In order to obtain the energetically-lowest mean-field solution, it is necessary that the ansatz for the wave function is of the most general mean-field form. Due to the variational principle, the minimization of the respective energy functional with respect to all parameters of the ansatz wave function will then give the *best* solution within mean-field theory. It is therefore legitimate to call this mean-field solution the best mean field (BMF). A procedure to obtain the best mean-field (BMF) solution numerically has been developed recently [25–28, 33].

In the best mean-field approach the ansatz for the wave function  $|\Psi\rangle$  is taken as a single permanent of  $N$  bosons distributed over  $M$  time-independent orthonormal orbitals  $\phi_k(\mathbf{r})$ :

$$|\Psi\rangle = |n_1, n_2, \dots, n_M\rangle. \quad (21)$$

Using this ansatz for the wave function, the energy functional is minimized by a variation over the number of orbitals  $M$ , the occupation numbers  $n_i$  and the orbitals  $\phi_k(\mathbf{r})$  themselves [25, 28]. The variation leads to a set of coupled non-linear equations that have to be solved to obtain the BMF solution. Thereby, the energetically most favourable permanent is selected to approximate the true many-body wave function. The GP mean-field is contained in the BMF ansatz as can be seen by restricting the number of orbitals to  $M = 1$ .

#### IV. A MODEL AND ITS PHYSICS

In order to examine correlation functions of Bose-condensed systems, we now turn to a specific example. For simplicity we work in one dimension,  $D = 1$ , and henceforth we substitute  $\mathbf{r} = x$  and  $\mathbf{k} = k$ . We will study the correlation functions of  $N = 1000$  repulsively interacting bosons in a double-well trap at various barrier heights. The dynamics of a similar system has been investigated recently in the context of a dynamically raised barrier [30]. In order to isolate physical effects that are due to the trapping geometry and not due to dynamical parameters such as the rate at which the barrier is raised, etc., we restrict our discussion to the ground state at different barrier heights. The restriction to a stationary state allows us to omit the time argument in all physical quantities from now on. Double-well systems have the interesting property that depending on the height of the barrier and/or the

interaction strength, the ground state undergoes a transition from a single to a fragmented condensate [24, 26, 28, 29]. We shall show how this transition from a condensed state to a fragmented condensate manifests itself in the correlation functions.

We work with a dimensionless Hamiltonian of the form

$$H = \sum_{i=1}^N \left( -\frac{1}{2} \frac{\partial^2}{\partial x_i^2} + V(x_i) \right) + \lambda_0 \sum_{i<j}^N \delta(x_i - x_j), \quad (22)$$

to solve the stationary Schrödinger equation  $H\Psi = E\Psi$ . All quantities in Eq. (22) are dimensionless and the connection to a dimensional Hamiltonian

$$\tilde{H} = \sum_{i=1}^N \left( -\frac{\hbar^2}{2m} \frac{\partial^2}{\partial \tilde{x}_i^2} + \tilde{V}(\tilde{x}_i) \right) + \tilde{\lambda}_0 \sum_{i<j}^N \delta(\tilde{x}_i - \tilde{x}_j) \quad (23)$$

is made by the relations  $x_i = \tilde{x}_i/L$ , where  $L$  is a length scale,  $V(x_i) = \frac{mL^2}{\hbar^2} \tilde{V}(Lx_i)$ ,  $\lambda_0 = \frac{mL}{\hbar^2} \tilde{\lambda}_0$ ,  $\Psi(x_1, \dots, x_N) = \tilde{\Psi}(x_1L, \dots, x_NL)$  and  $E = \tilde{E} \frac{mL^2}{\hbar^2}$ . As an external potential we choose a harmonic trap with an additional central barrier of variable height  $V(x_i) = \frac{1}{2}x_i^2 + Ae^{(\frac{-x_i^2}{2\sigma^2})}$ , where  $A$  is the height of the potential barrier and  $\sigma = 2$  a fixed width. For the strength of the dimensionless interparticle interaction we choose  $\lambda_0 = 0.01$ . In the computations using MCTDHB we restrict the number of orbitals to  $M = 2$ , yielding a total of  $\binom{N+M-1}{N} = 1001$  permanents.

### A. Condensed state

We begin with a discussion of the ground state energy as a function of the barrier height. The ground state energy per particle of the many-body solution,  $E_{MCTDHB}/N$  (blue), is shown in Fig. 1 (top).  $E_{MCTDHB}/N$  increases with the height of the central barrier. The energy differences per particle of the many-body and the BMF solution with respect to the GP solution,  $(E_{MCTDHB} - E_{GP})/N$  (blue) and  $(E_{BMF} - E_{GP})/N$  (red), are shown in the inset of Fig. 1 (top). The energy difference  $(E_{MCTDHB} - E_{GP})/N$  is negative, because the interacting system can lower its energy by depleting the condensate. At low barrier heights the GP mean-field is the best mean-field and thus  $(E_{BMF} - E_{GP})/N = 0$ . A comparison of the energy scales of Fig. 1 and its inset reveals that the energy of the many-body solution, the BMF solution and the GP solution are very close at all barrier heights. The nature of the many-body ground state at different barrier heights varies nevertheless very strongly, as we shall show below.

Fig. 1 (middle) shows the occupations  $n_1^{(1)}/N$  and  $n_2^{(1)}/N$  of the first and second natural orbitals of the many-body wave function as a function of the barrier height, computed with MCTDHB. The largest eigenvalue of the first-order RDM,  $n_1^{(1)}$ , is only restricted by Eq. (5) and can therefore take on any value between 0 and  $N$ . The dashed lines indicate these upper and lower bounds on  $n_1^{(1)}$ . At low barrier heights only one natural orbital is significantly occupied. Therefore, we refer to the parameter range  $0 \leq A \leq 13$  as the condensed regime, in accordance with the definition of Penrose and Onsager [22]. The occupation of the second natural orbital is due to the two-body interaction between the particles. However, it remains below 1% for all values of the barrier height  $A \leq 13$  and is even below 10% at  $A = 0$ .

Since  $n_1^{(1)} \approx N$  in the condensed regime, the upper and the lower bounds, Eqs. (5) and (6), on the largest eigenvalue of the second-order RDM,  $n_1^{(2)}$ , are almost identical. Therefore,  $n_1^{(2)}$  is constrained to take on a value very close to  $N(N-1)$ . Consequently, there can be only one significantly occupied natural geminal. This is confirmed in Fig. 1 (bottom), where the natural geminal occupations are shown as a function of the barrier height. For the purpose of describing first- and second-order correlations it is therefore legitimate to approximate the many-body wave function in this regime by a single permanent  $|N, 0\rangle$  in which all  $N$  bosons occupy the first natural orbital  $\alpha_1^{(1)}(x_1)$ .

The first column of Fig. 2 shows the first (red) and the second (blue) natural orbitals of the many-body solution at barrier heights  $A = 0, 13, 19, 24$ , from top to bottom. The first and the second natural orbitals are symmetric and antisymmetric about the origin, respectively. At  $A = 0$  the first natural orbital,  $\alpha_1^{(1)}(x_1)$ , takes on the shape of a broadened Gaussian, reflecting the repulsive interaction between the particles. The second natural orbital,  $\alpha_2^{(1)}(x_1)$ , has a higher kinetic energy than the first one due to the node at the center of the trap. Additionally, the second natural orbital forces the particles to occupy regions of the trap where the trapping potential is higher. There is an energy gap between the one-particle energies of the first and second natural orbital. The occupation of the second natural orbital is therefore very small in the purely harmonic trap at the chosen interaction strength.

As the barrier height is varied from  $A = 0$  up to  $A = 13$ , the natural orbitals deform to fit the new shape of the external potential. The central peak of the first natural orbital splits into two maxima which become localized at positions  $x_1 = \pm d/2$ , where  $d$  is the distance between the wells of the external potential.

At the center of the trap, where the barrier is raised, the first natural orbital develops a local minimum in order to minimize the potential energy. The second natural orbital on the other hand has a node at the center of the trap at any barrier height. Its maximum and minimum are localized at the minima of the external potential. As the barrier is raised, the energy gap between the first two natural orbitals decreases. However, the increase of the depletion of the condensate from  $n_2^{(1)}/N < 1\%$  at  $A = 0$  to  $n_2^{(1)}/N \approx 1\%$  at  $A = 13$  cannot be explained in this single particle picture. On a single particle level the ground state would be fully condensed at any finite barrier height, i.e.  $n_2^{(1)} = 0$ . The reason for the observed increase in the depletion lies in the fact that for repulsively interacting many-boson systems in multi-well setups it becomes energetically more favourable to fragment as the barrier between the wells is raised [24, 26, 28, 29, 33]. The increase in energy which results from the occupation of orbitals with a higher one-particle energy can be outweighed by a decrease in interaction energy. This effect becomes dominant at barrier heights above  $A = 13$ , see Secs. IV B and IV C.

The second to fourth column of Fig. 2 show (from left to right) the first three natural geminals  $\alpha_i^{(2)}(x_1, x_2)$  at the same barrier heights as above. By expanding the natural geminals in the one-particle basis of natural orbitals one finds that the natural geminals in the condensed regime are approximately given by symmetrized products of the natural orbitals:

$$|\alpha_1^{(2)}\rangle = |2, 0\rangle, \quad |\alpha_2^{(2)}\rangle = |1, 1\rangle, \quad |\alpha_3^{(2)}\rangle = |0, 2\rangle, \quad (24)$$

where  $|m_1, m_2\rangle$  denotes a state with  $m_1$  particles in the first and  $m_2$  particles in the second natural orbital. Only the first natural geminal,  $\alpha_1^{(2)}(x_1, x_2)$ , is significantly occupied in the condensed regime. Due to the two-body interaction between the particles there is a small occupation of the second and third natural geminal. However, at low barrier heights their occupation is largely suppressed, due to the gap between the single particle energies of the first and second natural orbital. Since the geminals  $\alpha_2^{(2)}(x_1, x_2)$  and  $\alpha_3^{(2)}(x_1, x_2)$  contain the second natural orbital in their expansion, see Eq. (24), their occupation increases the total energy at low barrier heights.

In the equation for the energy expectation value, Eq. (8), the only substantially contributing natural geminal is  $\alpha_1^{(2)}(x_1, x_2)$ . The shape of  $\alpha_1^{(2)}(x_1, x_2)$  is particularly interesting. It has four maxima of similar height, located at positions  $x_1 = x_2 = \pm d/2$  and  $x_1 = -x_2 = \pm d/2$ , see the second panel in the second row of Fig. 2. Since  $\alpha_1^{(2)}(x_1, x_2)$  has peaks on the diagonal

at  $x_1 = x_2 = \pm d/2$ , it contributes to both, the one-particle part and the interaction part of the energy.

In contrast to the first natural geminal,  $\alpha_2^{(2)}(x_1, x_2)$  and  $\alpha_3^{(2)}(x_1, x_2)$  both exhibit node lines going through the region where the central barrier is raised. As the energy gap between the single particle energies of the natural orbitals  $\alpha_1^{(1)}(x_1, x_2)$  and  $\alpha_2^{(1)}(x_1, x_2)$  decreases, so does the energy gap between the natural geminals. Similar to the discussion of the natural orbital occupations above, this argument in terms of an energy gap does not explain the increase of the occupation of the second and third natural geminal when the barrier is raised. Without interactions the occupation numbers of all but the first natural geminal would be exactly zero.

We shall demonstrate in Sec. IV C that fragmented states allow the occupation of geminals that contribute very little to the interaction energy as opposed to condensed states. Thereby, the system can lower its energy, once the barrier is high enough.

## B. From condensation to fragmentation

At barrier heights  $13 < A < 24$ , one finds that the occupation of the second natural orbital  $n_2^{(1)}/N$  increases continuously from below 1% to almost 50%. The condensate fragments in this regime according to the definition of fragmented condensates [23]. In this regime many permanents contribute to the wave function and, therefore, we refer to the range of barrier heights  $13 < A < 24$  as the many-body regime. Along with the natural orbital occupations the natural geminal occupations change as well. Three natural geminals become occupied with increasing barrier height, see Fig. 1.

In the many-body regime, the upper and lower bounds, Eqs. (5) and (6), on the largest eigenvalue of the second-order RDM,  $n_1^{(2)}$ , no longer restrict  $n_1^{(2)}$  to a narrow region. In fact,  $n_1^{(2)}$  takes on a value somewhere in between these bounds.

This onset of fragmentation manifests itself also in the BMF solution which jumps from a GP type permanent  $|N, 0\rangle$  in the condensed regime to a fully fragmented solution of the form  $|N/2, N/2\rangle$ . Note that already at barrier heights  $A \geq 14$  this fragmented solution is lower in energy than a GP type permanent. At this barrier height the many-body solution is only slightly depleted, see Fig. 1.

If we compare the natural orbitals in Fig. 2 at barrier height  $A = 19$  with those at  $A = 13$ ,

we note that they look very similar, apart from the fact that the peaks are slightly farther apart, and the first natural orbital is closer to zero at the center of the trap. The energies of the first two natural orbitals are almost degenerate and the total energy is minimized by the occupation of both natural orbitals. Without interactions the system would remain in a condensed state, since the single particle energies of the first and the second natural orbitals remain separated at any finite barrier height. Note that in the absence of interactions the natural orbitals are the eigenfunctions of  $\hat{h}$ . However, as we noted in Sec. IV A, a system of repulsively interacting bosons in multi-well traps can lower its energy by occupying several natural orbitals, once the barrier is high enough [26–29, 33]. This is precisely the reason for the observed onset of fragmentation.

In the many-body regime the natural geminals are no longer symmetrized products of the natural orbitals. If we compare  $\alpha_1^{(2)}(x_1, x_2)$  in Fig. 2 at barrier heights  $A = 13$  and  $A = 19$ , we see that the peaks on the diagonal at  $x_1 = x_2 = \pm d/2$  decrease, whilst the peaks on the off-diagonal at  $x_1 = -x_2 = \pm d/2$  increase when the barrier is raised. The opposite is true for the third natural geminal  $\alpha_3^{(2)}(x_1, x_2)$ : the off-diagonal maxima at  $x_1 = -x_2 = \pm d/2$  have decreased, whilst the diagonal minima at  $x_1 = x_2 = d/2$  are now more negative. On the other hand, the second natural geminal,  $\alpha_2^{(2)}(x_1, x_2)$ , is still well approximated by a symmetrized product of the first and second natural orbital. The behavior of the natural geminals is qualitatively different from that displayed by the natural orbitals. In contrast to the natural orbitals, the natural geminals *do* change their shape during the fragmentation transition. They only obtain their final forms, when the fragmentation transition is completed, see Fig. 2 and Sec. IV C. It is possible to understand qualitatively which of the two unoccupied natural geminals becomes occupied first. In the condensed regime  $\alpha_2^{(2)}(x_1, x_2)$  is well approximated by a state  $|1, 1\rangle$  in which one boson occupies the first natural orbital and another one the second natural orbital, see Eq. (24). Meanwhile,  $\alpha_3^{(2)}(x_1, x_2)$  is well approximated by a state  $|0, 2\rangle$ , in which two bosons reside in the second natural orbital. Since the single particle energies of the first and second natural orbitals are separated, the occupation of the third natural geminal costs more energy than that of the second. Hence the second natural geminal becomes occupied before the third, see Fig. 1 (bottom).



### C. Fully fragmented state

When the central barrier is raised to values  $A \geq 24$ , the two parts of the condensate become truly independent. The natural orbital occupations approach  $n_1^{(1)} = n_2^{(1)} = N/2$ , which reflects the fact that the energies associated with the first and second natural orbitals degenerate at infinite barrier heights. The many body wave function can then be adequately approximated by a single permanent of the form  $|N/2, N/2\rangle$ , i.e. with equal numbers of particles in the first and the second natural orbitals. Therefore, we refer to barrier heights  $A \geq 24$  as the fully fragmented regime. The additional energy, necessary for the occupation of the second natural orbital, is outweighed by a lower interaction energy. Note that this final form of the wave function is anticipated by the BMF solution at barrier heights  $A \geq 14$ .

The natural geminal occupations approach

$$n_1^{(2)} = N(N/2), \quad n_2^{(2)} = n_3^{(2)} = N/2(N/2 - 1) \quad (25)$$

in the fully fragmented regime. These are the values that follow from the BMF solution.

It is only at barrier heights  $A \geq 24$  that the natural geminals take on their final shapes, compare the third and fourth rows of Fig. 2. If we expand the natural geminals in the basis of natural orbitals at these barrier heights, we find that

$$|\alpha_1^{(2)}\rangle = \frac{1}{\sqrt{2}} (|2, 0\rangle - |0, 2\rangle), \quad |\alpha_2^{(2)}\rangle = |1, 1\rangle, \quad |\alpha_3^{(2)}\rangle = \frac{1}{\sqrt{2}} (|2, 0\rangle + |0, 2\rangle) \quad (26)$$

holds to a very good approximation. The first and third natural geminals have equal contributions coming from the first and the second natural orbitals. The question arises, why their occupations are different, about 50% and 25%, respectively. Subtracting the permanents  $|2, 0\rangle$  and  $|0, 2\rangle$  from one another yields a geminal which is localized on the *off-diagonal*, see  $\alpha_1^{(2)}(x_1, x_2)$  in Fig. 2 at  $A = 24$ . Adding the permanents  $|2, 0\rangle$  and  $|0, 2\rangle$  yields a geminal which is localized on the *diagonal*, see  $\alpha_3^{(2)}(x_1, x_2)$  in Fig. 2 at  $A = 24$ . It is easy to see from the shape of the natural geminals in the fourth row of Fig. 2 that the integrals over the one-body part in Eq. (8) are approximately the same for each of the natural geminals. Given the occupations in Eq. (25), the first natural geminal contributes about one half of the one-body energy, whereas the second and the third natural geminal contribute about a fourth each. The situation is different for the two-body part of the Hamiltonian. Since  $\alpha_2^{(2)}(x_1, x_2)$  and  $\alpha_3^{(2)}(x_1, x_2)$  are localized on the diagonal, they *do* contribute to the interaction energy. In contrast,  $\alpha_1^{(2)}(x_1, x_2)$  is almost zero at coordinate values  $x_1 \approx x_2$  and, due

to the contact interaction in Eq. (23), it practically does not contribute to the interaction energy. At high barriers a fragmented state allows the system to lower its energy through the occupation of a natural geminal which is localized on the off-diagonal.

We would like to make a remark on the validity of the present MCTDHB computation for high barriers. For high barriers the whole system can be considered as composed of two separate condensates. To describe the depletion of each condensate it would be necessary to employ  $M = 4$  orbitals. We use only  $M = 2$  orbitals in the many-body computation and cannot describe this depletion. We justify the use of  $M = 2$  orbitals by noting that at  $A = 0$  the system is almost fully condensed, and the depletion can be safely neglected, see Fig. 1. Therefore, we assume that the depletion of each of the two condensates can be neglected, when the barrier is very high. This claim is supported by a computation that we carried out in the harmonic trap at the same interaction strength  $\lambda_0 = 0.01$  for 500 particles. The depletion was found to be even less than for  $N = 1000$  particles.

## V. FIRST ORDER CORRELATIONS

### A. General analytical considerations

We now describe the first-order correlations in an analytical mean-field model for the two limiting cases of a condensed and a fully fragmented system. In these cases mean-field theory has been shown to be well applicable, see Sec. IV. For our purposes the exact shape of the natural orbitals  $\alpha_1^{(1)}(x_1)$  and  $\alpha_2^{(1)}(x_1)$  is unimportant. Consider a normalized one-particle function,  $\Phi(x)$ , which is localized at the origin.  $\Phi(x)$  may vary in shape, but is always assumed to resemble a Gaussian. Similarly, we define translated copies  $\Phi_1(x) = \Phi(x + d/2)$  and  $\Phi_2(x) = \Phi(x - d/2)$  of  $\Phi(x)$ , where the previously defined distance  $d$  between the minima of the potential wells is taken to be large enough to set products of the form  $\Phi_1(x)\Phi_2(x)$  to zero. Since  $\Phi$  is localized in some region around the origin,  $\Phi_1$  is localized in a region  $L$  to the left and  $\Phi_2$  in a region  $R$  to the right of the origin.

#### 1. Condensed state

In the condensed regime,  $0 \leq A \leq 13$ , only one natural orbital,  $\alpha_1^{(1)}(x_1)$ , is significantly occupied. Therefore, we approximate the first-order reduced density operator of the system

by that of a condensed state  $|N, 0\rangle$

$$\hat{\rho}_{|N,0\rangle}^{(1)} = N|\alpha_1^{(1)}\rangle\langle\alpha_1^{(1)}|. \quad (27)$$

It then follows from Eq. (13) that

$$|g_{|N,0\rangle}^{(1)}(x'_1, x_1)|^2 = 1. \quad (28)$$

At zero barrier height, the first natural orbital is a Gaussian, broadened by interactions. Therefore, we write  $\alpha_1^{(1)}(x_1) = \Phi(x_1)$ , and hence the one-particle density distribution and the one-particle momentum distribution are of the form

$$\rho_{|N,0\rangle}^{(1)}(x_1|x_1) = N|\Phi(x_1)|^2, \quad (29)$$

$$\rho_{|N,0\rangle}^{(1)}(k_1|k_1) = N|\Phi(k_1)|^2. \quad (30)$$

Since  $\Phi(x_1)$  is a broadened Gaussian, its Fourier transform  $\Phi(k_1)$  is also close to a Gaussian, but narrower in comparison to a non-interacting system. The momentum distribution of the repulsively interacting system in the harmonic trap is therefore narrower than that of a non-interacting system.

We now turn to the case corresponding to  $A \approx 13$ , where the system is still condensed, but the first two natural orbitals are spread out over the two wells. We model the natural orbitals by

$$\alpha_1^{(1)}(x_1) = \frac{1}{\sqrt{2}} [\Phi_1(x_1) + \Phi_2(x_1)], \quad \alpha_2^{(1)}(x_1) = \frac{1}{\sqrt{2}} [\Phi_1(x_1) - \Phi_2(x_1)]. \quad (31)$$

In this case one obtains [56]:

$$\rho_{|N,0\rangle}^{(1)}(x_1|x_1) = \frac{N}{2} |\Phi_1(x_1)|^2 + \frac{N}{2} |\Phi_2(x_1)|^2, \quad (32)$$

$$\rho_{|N,0\rangle}^{(1)}(k_1|k_1) = N[1 + \cos(k_1 d)] |\Phi(k_1)|^2 \quad (33)$$

for the density and the momentum distribution. We note that the one-particle momentum distribution displays an oscillatory pattern in momentum space at a period which is determined by the separation  $d$  of the centers of the two wells.

## 2. Fully fragmented state

In the true many-body regime,  $13 < A < 24$ , where many permanents contribute to the wave function, a mean-field model is bound to fail. However, in the fully fragmented regime it

is possible to consider the whole system as two separate condensates, and hence a mean-field description is again applicable. Therefore, we now turn to the case corresponding to  $A \geq 24$ , where the system is fully fragmented and the many-body state is given by  $|N/2, N/2\rangle$ . The first-order density operator then reads:

$$\hat{\rho}_{|N/2, N/2\rangle}^{(1)} = \frac{N}{2} |\alpha_1^{(1)}\rangle \langle \alpha_1^{(1)}| + \frac{N}{2} |\alpha_2^{(1)}\rangle \langle \alpha_2^{(1)}|. \quad (34)$$

Since the natural orbitals remain qualitatively unchanged during the fragmentation transition, we approximate  $\alpha_1^{(1)}(x_1)$  and  $\alpha_2^{(1)}(x_1)$  by Eqs. (31) and obtain for the density and the momentum distribution [56]:

$$\rho_{|N/2, N/2\rangle}^{(1)}(x_1|x_1) = \frac{N}{2} |\Phi_1(x_1)|^2 + \frac{N}{2} |\Phi_2(x_1)|^2, \quad (35)$$

$$\rho_{|N/2, N/2\rangle}^{(1)}(k_1|k_1) = N |\Phi(k_1)|^2. \quad (36)$$

We note that the one-particle momentum distribution of independent condensates does not contain an oscillatory component and is identical to the momentum distribution of a single, localized condensate of  $N$  particles within this model, see Eq. (30). For the normalized first-order correlation function one finds

$$|g_{|N/2, N/2\rangle}^{(1)}(x'_1, x_1)|^2 = \begin{cases} 1 & \text{if } x_1, x'_1 \in L \text{ or } x_1, x'_1 \in R, \\ 0 & \text{otherwise.} \end{cases} \quad (37)$$

Whereas the state  $|N, 0\rangle$  is fully first-order coherent, the fragmented state  $|N/2, N/2\rangle$  is only first-order coherent in a restricted and generally disconnected region. Each of the two condensates is first-order coherent, but the mutual coherence which is present in the condensed regime is lost.

## B. Numerical results

We now turn to the discussion of first-order correlations. In particular, we are interested in effects that are due to the true many-body nature of the wave function. Along with our many-body results we plot the corresponding results of the BMF solution. From the discussion in Sec. IV it is clear that we expect many-body effects to occur during the fragmentation transition at barrier heights  $13 < A < 24$ . In the condensed and in the fully fragmented regime we expect that the many-body results are well approximated by those of the BMF

solution. In these cases we can understand the structure of the correlation functions on the basis of the analytical mean-field model of Sec. V A.

The first column of Fig. 3 shows the one-particle density distribution  $\rho^{(1)}(x_1|x_1)$  of the many-body solution (blue line) and that of the BMF solution (red line with triangles) at the barrier heights  $A = 0, 13, 19, 24$ , from top to bottom. It is remarkable that the one-particle densities obtained from either the many-body wave function or the BMF solution give results that cannot be distinguished from one another at *any* barrier height.

In a purely harmonic trap,  $A = 0$ , the one-particle density takes on the form of an interaction-broadened Gaussian. At higher barriers, the density splits into two parts that are localized in each of the wells. At  $A = 13$ , the one-particle density has developed two separated peaks. Note that the system is still in the condensed regime at this barrier height and must be considered a single condensate, despite the spatial separation between the two peaks.

When the central barrier is raised further to values  $13 < A < 24$  the condensate fragments, see Fig. 1. At a barrier height of  $A = 19$  the system is halfway on its way from a condensed to a fully fragmented condensate. Many permanents contribute to the many-body wave function and one may wonder how this transition manifests itself in observable quantities. However, apart from a small shift of the center of the two peaks and a reduction at the center of the trap,  $\rho^{(1)}(x_1|x_1)$  remains largely unaffected by this transition. If the barrier is raised further to  $A = 24$ , the fragmentation transition is largely completed. Also during the transition from a true many-body state to a fully fragmented state there is no visible indication of this transition in the one-particle density.

The second column of Fig. 3 shows the one-particle momentum distribution  $\rho^{(1)}(k_1|k_1)$  at the same barrier heights as before. At  $A = 0$ , the one-particle momentum distribution is given by a squeezed Gaussian, in agreement with Eq. (30). At  $A = 13$  the one-particle momentum distribution has developed an oscillatory pattern, typical of a single condensate spread out over two wells. The structure of  $\rho^{(1)}(k_1|k_1)$  is well reproduced by Eq. (33) of the analytical mean-field model. Up to this barrier height the BMF solution is almost identical to the many-body wave function, and therefore the respective momentum distributions are indistinguishable, see the two upper panels in the second column of Fig. 3.

When the system enters the many-body regime,  $13 < A < 24$ , the momentum distribution of the many-body solution deforms to a Gaussian-like envelope, modulated by an oscillatory

part. The BMF momentum distribution, on the other hand, already takes on the form characteristic of two separate condensates. It agrees with the prediction of Eq. (36), which is clearly different from the many-body result. This merely reflects the fact that the exact wave function is inaccessible to mean-field methods in the many-body regime.

When the state becomes fully fragmented at  $A = 24$ , the many-body momentum distribution and the BMF momentum distribution become indistinguishable again, consistent with an explanation in terms of two independent condensates, see Eq. (36). Compared to  $\rho^{(1)}(k_1|k_1)$  at  $A = 0$ , the momentum distribution is broader at  $A = 24$ , because the density distribution in each of the two wells is narrower than that in the harmonic trap.

The third column of Fig. 3 shows the absolute value squared of the normalized first-order correlation function  $|g^{(1)}(x'_1, x_1)|^2$  of the many-body solution only. Here and in all following graphs of correlation functions we restrict the plotted region by a simple rule. To avoid analyzing correlations in regions of space where the density is essentially zero, we plot the respective correlation function only in regions where the density is larger than 1% of the maximum value of the density in the entire space. We apply the same rule also in momentum space.

At zero barrier height  $|g^{(1)}(x'_1, x_1)|^2$  is very close to one in the region where the density is localized. The system is first-order coherent to a very good approximation and the mean-field formula Eq. (28) applies. As the barrier is raised to  $A = 13$  the coherence between the two peaks, e.g. at  $x_1 = -x'_1$ , is slightly decreased, while the coherence within each of the peaks is preserved. Note that the density at the center of the trap is already below 1% of the maximal value in this case. Despite this separation the system remains largely condensed, but deviations from Eq. (28) are visible. If the barrier is raised further to  $A = 19$ , the coherence of the system on the off-diagonal decreases quickly. Although the bosons in each well remain coherent among each other, the overall system is only partially coherent. At barrier heights  $A \geq 24$ , the coherence between the two wells is entirely lost. This is also the scenario that the BMF solution anticipates, see Eq. (37).

It is remarkable that not only the density, but also the momentum distribution obtained within mean-field theory agree so well with the many-body result, when the system is not in the true many-body regime. This would not be the case if we had restricted the mean-field approach to the GP equation, as we shall show now.

Up to barrier heights  $A = 13$  the many-body system is condensed, and the BMF solution

coincides with the GP solution. The BMF, and therefore also the GP solution provide good approximations to the interacting many-body system. Above  $A = 13$  the results obtained with the GP mean-field become qualitatively wrong as the barrier is raised. To illustrate this point, we plot the GP results corresponding to those of Fig. 3 at barrier heights  $A = 19$  (top) and  $A = 24$  (bottom) in Fig. 4. A comparison of the respective one-particle densities, shown in the first column of Fig. 3 and Fig. 4, reveals no visible difference. The GP mean-field reproduces the density distribution at all barrier heights correctly. However, the GP solution fails at the description of the momentum distribution and the normalized first order correlation function, compare the second and third columns of Figs. 3 and 4 at the same barrier heights. The reason for the failure of the GP mean-field is the assumption that all bosons occupy the same orbital. It is by construction incapable to describe fragmented condensates.

## VI. SECOND ORDER CORRELATIONS

### A. General analytical considerations

In this subsection we extend the analytical mean-field model of Sec. V A to describe second-order correlations.

#### 1. Condensed state

We found in Sec. IV A that only one natural geminal is significantly occupied in the condensed regime, where the many-body state is approximately given by a single permanent in which all bosons occupy the same single particle state. Therefore, we approximate the second order reduced density operator in the condensed regime by that of the state  $|N, 0\rangle$ :

$$\hat{\rho}_{|N,0\rangle}^{(2)} = N(N-1)|\alpha_1^{(2)}\rangle\langle\alpha_1^{(2)}|, \quad (38)$$

where  $\alpha_1^{(2)}(x_1, x_2) = \alpha_1^{(1)}(x_1)\alpha_1^{(1)}(x_2)$  is the permanent in which two bosons reside in the first natural orbital  $\alpha_1^{(1)}$ . For the condensed state  $|N, 0\rangle$  one finds that up to corrections of order

$\mathcal{O}(1/N)$  the state is second-order coherent:

$$g_{|N,0\rangle}^{(2)}(x_1, x_2, x_1, x_2) = 1 - \frac{1}{N}, \quad (39)$$

$$g_{|N,0\rangle}^{(2)}(k_1, k_2, k_1, k_2) = 1 - \frac{1}{N}. \quad (40)$$

Thus, there are practically no two-body correlations if  $N \gg 1$ . At zero barrier height the first natural orbital takes on the shape of a broadened Gaussian,  $\alpha_1^{(1)}(x_1) = \Phi(x_1)$ , where  $\Phi(x)$  is defined in Sec. V A. The first natural geminal then reads  $\alpha_1^{(2)}(x_1, x_2) = \Phi(x_1)\Phi(x_2)$ . It follows that the two-particle density and the two-particle momentum distribution factorize up to corrections of order  $\mathcal{O}(1/N)$  into products of the respective one-particle distributions:

$$\rho_{|N,0\rangle}^{(2)}(x_1, x_2|x_1, x_2) = N(N-1)|\Phi(x_1)|^2|\Phi(x_2)|^2, \quad (41)$$

$$\rho_{|N,0\rangle}^{(2)}(k_1, k_2|k_1, k_2) = N(N-1)|\Phi(k_1)|^2|\Phi(k_2)|^2. \quad (42)$$

At the barrier height  $A = 13$ , the system is condensed but spread out over the two wells. Then, using Eqs. (31) to approximate  $\alpha_1^{(1)}$ , we find

$$\begin{aligned} \rho_{|N,0\rangle}^{(2)}(x_1, x_2|x_1, x_2) = \frac{N(N-1)}{4} [ & |\Phi_1(x_1)\Phi_1(x_2)|^2 + |\Phi_1(x_1)\Phi_2(x_2)|^2 + \\ & |\Phi_2(x_1)\Phi_1(x_2)|^2 + |\Phi_2(x_1)\Phi_2(x_2)|^2 ], \end{aligned} \quad (43)$$

$$\rho_{|N,0\rangle}^{(2)}(k_1, k_2|k_1, k_2) = N(N-1)[1 + \cos(k_1 d)][1 + \cos(k_2 d)]|\Phi(k_1)\Phi(k_2)|^2 \quad (44)$$

for the two-particle density and the two-particle momentum distribution. Apart from a correction of order  $\mathcal{O}(1/N)$ , the two-particle density and the two-particle momentum distribution are again products of the respective one-particle distributions.

## 2. Fully fragmented state

In Sec. IV C we found that three natural geminals are occupied in the fully fragmented regime, see Eq. (25). The occupations of Eq. (25) hold exactly for a state of the form  $|N/2, N/2\rangle$ . Therefore, we approximate the second-order reduced density operator in the fully fragmented regime by that of the state  $|N/2, N/2\rangle$ :

$$\hat{\rho}_{|N/2, N/2\rangle}^{(2)} = N \frac{N}{2} |\alpha_1^{(2)}\rangle\langle\alpha_1^{(2)}| + \frac{N}{2} \left( \frac{N}{2} - 1 \right) |\alpha_2^{(2)}\rangle\langle\alpha_2^{(2)}| + \frac{N}{2} \left( \frac{N}{2} - 1 \right) |\alpha_3^{(2)}\rangle\langle\alpha_3^{(2)}|, \quad (45)$$

where the natural geminals  $|\alpha_i^{(2)}\rangle$  are given by Eq. (26). In contrast to the condensed state, the normalized second-order correlation function of the fully fragmented state has a more



complicated structure due to the different terms contributing to Eq. (45). We approximate the natural geminals using Eqs. (31) and find

$$\begin{aligned} \rho_{|N/2, N/2\rangle}^{(2)}(x_1, x_2 | x_1, x_2) &= \frac{N}{2} \left( \frac{N}{2} - 1 \right) [|\Phi_1(x_1)\Phi_1(x_2)|^2 + |\Phi_2(x_1)\Phi_2(x_2)|^2] + \\ &\quad \frac{N}{2} \frac{N}{2} [|\Phi_1(x_1)\Phi_2(x_2)|^2 + |\Phi_2(x_1)\Phi_1(x_2)|^2], \end{aligned} \quad (46)$$

$$\rho_{|N/2, N/2\rangle}^{(2)}(k_1, k_2 | k_1, k_2) = N(N-1) \left( 1 + \frac{N}{N-1} \frac{\cos[(k_1 - k_2)d]}{2} \right) |\Phi(k_1)\Phi(k_2)|^2 \quad (47)$$

for the two-particle density and the two-particle momentum distribution. This representation allows us to identify the first two terms in Eq. (46) as contributions coming from two separate condensates of  $N/2$  bosons each, with condensate wave functions  $\Phi_1(x_1)$  and  $\Phi_2(x_1)$ . The third term in Eq. (46) is due to the fact that the bosons in the two separated condensates are identical particles. For the normalized second-order correlation function one finds:

$$g_{|N/2, N/2\rangle}^{(2)}(x_1, x_2, x_1, x_2) = \begin{cases} 1 - \frac{2}{N} & \text{if } x_1, x_2 \in L \text{ or } x_1, x_2 \in R \\ 1 & \text{otherwise} \end{cases}, \quad (48)$$

which mimics a high degree of second-order coherence. However, when  $g^{(2)}$  is evaluated on the diagonal in momentum space, one finds

$$g_{|N/2, N/2\rangle}^{(2)}(k_1, k_2, k_1, k_2) = \left( 1 - \frac{1}{N} \right) \left( 1 + \frac{N}{N-1} \frac{\cos[(k_1 - k_2)d]}{2} \right), \quad (49)$$

which displays an oscillatory behavior and deviates significantly from a uniform value of one. Hence the system is clearly not coherent, see Sec. II. Therefore, a description of second order correlations in terms of  $\rho^{(2)}(x_1, x_2 | x_1, x_2)$  and  $g^{(2)}(x_1, x_2, x_1, x_2)$  is incomplete, and  $\rho^{(2)}(k_1, k_2 | k_1, k_2)$  and  $g^{(2)}(k_1, k_2, k_1, k_2)$  have to be taken into account. Although this may seem obvious in the present case of a fully fragmented state, this reduction of coherence is more intricate in a state which is only partially fragmented, see following subsection.

## B. Numerical results

In this subsection we discuss the second-order correlations of the many-body solution. We compare the results to those of the BMF solution. When mean-field theory gives a good approximation to the many-body results, we also compare with the analytical mean-field model of Sec. VI A.

The first two columns of Fig. 5 show the two-particle density  $\rho^{(2)}(x_1, x_2|x_1, x_2)$  of the many-body (left) and BMF (right) solutions at barrier heights  $A = 0, 13, 19, 24$ , from top to bottom. At zero barrier height  $\rho^{(2)}(x_1, x_2|x_1, x_2)$  is localized at the center of the trap. The two-particle density factorizes approximately into a product of the one-particle densities:  $\rho^{(2)}(x_1, x_2|x_1, x_2) \approx \rho^{(1)}(x_1|x_1)\rho^{(1)}(x_2|x_2)$ . This remains true up to barrier heights  $A = 13$ , where the condensate is spread out over the two wells. The BMF result approximates the many-body result well in the condensed regime, and the structure of  $\rho^{(2)}(x_1, x_2|x_1, x_2)$  is that of Eqs. (41) and (43) at barrier heights  $A = 0$  and  $A = 13$ , respectively.

When the barrier is raised further to  $A = 19$ , the system fragments. Many permanents contribute to the wave function in this regime and there is no simple formula that relates the occupations of the natural orbitals to the two-particle density. Similar to the one-particle density, described in Sec. V B, the two-particle density seems to take no notice of the transition from a single to a fragmented condensate. It remains practically unchanged during the transition, apart from a slight shift of the peaks away from each other as the barrier is raised.

At even higher barriers,  $A \geq 24$ , the many-body state becomes fully fragmented and the wave function approaches  $|N/2, N/2\rangle$ . In this limit it is again possible to describe the two-particle density on a mean-field level. Therefore, the analytical results of Sec. VI A for the fully fragmented state should apply. In fact, the structure of  $\rho^{(2)}(x_1, x_2|x_1, x_2)$  in the fully fragmented regime is that predicted by Eq. (46).

The two-particle density of the condensed state just below the fragmentation transition and of the fully fragmented state above the fragmentation transition cannot be distinguished. It is easily verified, that Eqs. (43) and (46) give rise to the same two-particle density profile up to corrections of order  $\mathcal{O}(1/N)$ .

In contrast, the fragmentation transition is clearly visible in the two-particle momentum distribution. In the third and fourth columns of Fig. 5 the two-particle momentum distribution  $\rho^{(2)}(k_1, k_2|k_1, k_2)$  of the many-body (left) and BMF (right) wave function are shown.

In the condensed regime the two-particle momentum distribution is approximately given by the product of one-particle momentum distributions of a single condensate. This agrees with the analytical predictions of Eq. (42) at barrier height  $A = 0$  and Eq. (44) at  $A = 13$ . The mean-field picture is appropriate here.

In the many-body regime the two-particle momentum distribution  $\rho^{(2)}(k_1, k_2|k_1, k_2)$  contains contributions from many permanents. The resulting  $\rho^{(2)}(k_1, k_2|k_1, k_2)$  has a structure that lies somewhat in between the two results, Eqs. (44) and (47), obtained within the analytical mean-field model. The BMF solution is fully fragmented and does not provide an accurate approximation to the many-body two-particle momentum distribution in this regime, see Fig. 5, third and fourth columns in the third row from above.

When the barrier is raised to  $A = 24$ , the many-body state becomes fully fragmented and the mean-field picture is again applicable. The pattern of a single coherent condensate has now vanished completely in favor of a pattern characteristic of two separate condensates. The pattern agrees well with the structure predicted by Eq. (47).

Similar to our results on first order correlations, discussed in Sec. VB, the fragmentation transition shows up in the two-particle momentum distribution, but not in the two-particle density. While this behavior is predictable in the limiting cases of a condensed and a fully fragmented state, it is necessary to solve the many-body problem to determine the limits of such mean-field approximations. Particularly the behavior in between the two mean-field limits is only accessible to many-body approaches.

We will now address the second-order coherence of the system. The first two columns of Fig. 6 show the diagonal of the normalized second order correlation function  $g^{(2)}(x_1, x_2, x_1, x_2)$  of the many-body (left) and the BMF (right) solutions. Note the scale! The Eqs. (39) and (48) of the analytical mean-field model of Sec. VIA predict very small correlations in the two-particle density of the condensed and the fragmented state. This is confirmed in the first column of Fig. 6. In the condensed regime at zero barrier height the effects of the depletion of the condensate on  $g^{(2)}(x_1, x_2, x_1, x_2)$  are visible. Almost no two-particle density correlations are present. This is equally true in the case of a single condensate spread out over the two wells and also in the many-body regime. Above the fragmentation transition, the present computation of the many-body solution cannot describe effects on  $g^{(2)}$  that are due to the depletion of the condensate. However, since depletion effects are negligible in the harmonic trap, we are reassured that they are also negligible in the fully fragmented regime, see Sec. IV C. The BMF solution predicts almost identical two-body density correlations, see second column of Fig. 6.

On the basis of  $g^{(2)}(x_1, x_2, x_1, x_2)$  alone, the many-body state *appears* to be second-order coherent at all barrier heights. A high degree of second-order coherence requires Eq. (14)

to hold to a very good approximation for  $p = 1$  and  $p = 2$ . This in turn requires the largest eigenvalues of the first- and second-order RDM to be  $n_1^{(1)} \approx N$  and  $n_1^{(2)} \approx N(N-1)$ , respectively. We have already demonstrated in Sec. IV that these conditions are only satisfied in the condensed regime. Therefore, it is obviously tempting, but wrong to conclude from  $g^{(2)}(x_1, x_2, x_1, x_2) \approx 1$  that the system is second-order coherent. This misconception is due to the fact that  $g^{(2)}(x_1, x_2, x_1, x_2)$  only samples a small part of the first and second-order RDMs of the system.

So, how does the decrease of coherence manifest itself in second order correlation functions? For second-order coherence to be present, at least approximately, also  $g^{(2)}(k_1, k_2, k_1, k_2)$  has to be close to one. The third and fourth column of Fig. 6 show  $g^{(2)}(k_1, k_2, k_1, k_2)$  of the many-body (left) and BMF (right) solution. At zero barrier height the system is indeed highly second-order coherent since only one natural orbital is significantly occupied. Not only  $g^{(2)}(x_1, x_2, x_1, x_2)$ , but also  $g^{(2)}(k_1, k_2, k_1, k_2)$  is very close to one here. However, at  $A = 13$  when the many-body state is still condensed,  $g^{(2)}(k_1, k_2, k_1, k_2)$  starts to develop a structure.

When the barrier is raised to values above  $A = 13$ , the structure becomes more and more pronounced. In the many-body regime at  $A = 19$ , we find that  $g^{(2)}(k_1, k_2, k_1, k_2)$  has a complicated behavior and deviates significantly from values close to one, thereby proving that strong correlations are present. Note that the interaction between the particles is weak and that the strong correlations are due to the transition from a single to a fragmented condensate. This transition is in turn induced by a change of the shape of external potential. Varying the shape of the external potential therefore provides a means to introduce strong correlations between the particles. The strongest correlations (black spots in the third panel of the third row of Fig. 6) occur at those values where the two-body momentum distribution has local minima. At the values of  $k_1$  and  $k_2$ , where the strongest correlations occur, the one-body and the two-body momentum distributions are *clearly* distinct from zero, see third panel in the middle column of Fig. 3 and the third panel in the third row of Fig. 5. Experiments that measure  $g^{(2)}(k_1, k_2, k_1, k_2)$  in ultracold quantum gases have been carried out recently, see e.g. [57]. An experiment that measures  $g^{(2)}(k_1, k_2, k_1, k_2)$  would find strong two-particle momentum correlations at high barriers.

When the system becomes fully fragmented at barrier heights  $A \geq 24$  the structure of  $g^{(2)}(k_1, k_2, k_1, k_2)$  becomes more regular again. The amplitude of the correlations is smaller

than in the many-body regime, and the correlations between different momenta are modulated by a single oscillatory structure. This structure can be well understood within the analytical mean-field model of Sec. VI A. The oscillatory part of  $g^{(2)}(k_1, k_2, k_1, k_2)$  is determined by the difference of the wave vectors multiplied by the distance between the wells, see Eq. (49).

Hence, we find that only in the condensed regime the system is second-order coherent despite the fact that  $g^{(2)}(x_1, x_2, x_1, x_2) \approx 1$  at all barrier heights. This merely reflects the fact that  $g^{(2)}(x_1, x_2, x_1, x_2)$  is only the diagonal of  $g^{(2)}(x'_1, x'_2, x_1, x_2)$ . On the other hand,  $g^{(2)}(k_1, k_2, k_1, k_2)$  depends on all values of  $\rho^{(2)}(x_1, x_2|x'_1, x'_2)$  and provides complementary information about the coherence of the state. A description of second-order coherence in terms of  $g^{(2)}(x_1, x_2, x_1, x_2)$  alone is therefore incomplete.

The corresponding results of the BMF solution agree well with those of the many-body solution as long as the system is not in the many-body regime at intermediate barrier heights. In the many-body regime the BMF result is inaccurate, but it anticipates the final form of  $g^{(2)}(x_1, x_2, x_1, x_2)$  in the fragmented regime.

## VII. CONCLUSIONS

In this work we have investigated first- and second-order correlations of trapped interacting bosons. For illustration purposes we have investigated the ground state of  $N = 1000$  weakly interacting bosons in a one-dimensional double-well trap geometry at various barrier heights on a many-body level. We have obtained the many-body results by solving the many-body Schrödinger equation with the recently developed MCTDHB method. This allowed us to compute from first principles the natural orbitals and the natural geminals of a large interacting many-body system, together with their occupation numbers. To our knowledge this is the first computation of the natural geminals of an interacting many-body system of this size.

Depending on the height of the double-well barrier we found that there are three different parameter regimes. At low barriers the ground state is condensed and the many-body wave function is well approximated by a single permanent of the form  $|N, 0\rangle$ . At high barriers the ground state becomes fully fragmented and can be well approximated by a single permanent of the form  $|N/2, N/2\rangle$ . At intermediate barrier heights, where the transition from a single to

a fragmented condensate occurs, the ground state becomes a true many-body wave function to which many permanents contribute. We have demonstrated that the transition to a fragmented state results in the occupation of a natural geminal that contributes very little to the interaction energy. The overall energy of the system can be lowered by the occupation of such a geminal, and the ground state becomes fragmented.

We have shown how the transition from a condensed to a fully fragmented ground state manifests itself in the one- and two-particle momentum distributions. However, the transition is *not* captured by the one- and two-particle density distributions, not even in the many-body regime.

In order to determine the coherence of the state during the fragmentation transition, we have computed the first- and second-order normalized correlation functions  $g^{(1)}(x'_1, x_1)$ ,  $g^{(2)}(x_1, x_2, x_1, x_2)$  and  $g^{(2)}(k_1, k_2, k_1, k_2)$ . In the condensed regime, a high degree of coherence is indeed present in the ground state wave function. First and second order correlations were found to be negligible at the interaction strength and particle number chosen for our computation. However, with increasing barrier height correlations between the momenta of the particles build up. These correlations were found to be very strong in the many-body regime at intermediate barrier heights. The ground state at high barriers was found to be correlated, but not as strongly as the ground state at intermediate barrier heights.

While the transition from a virtually uncorrelated state to a correlated one is clearly visible in  $g^{(1)}(x'_1, x_1)$  and  $g^{(2)}(k_1, k_2, k_1, k_2)$ , the transition hardly shows up in  $g^{(2)}(x_1, x_2, x_1, x_2)$ . A description of second-order coherence in terms of  $g^{(2)}(x_1, x_2, x_1, x_2)$  alone is, therefore, incomplete and can lead to wrong predictions.

For comparison we have computed results based on (i) the best approximation of the many-body wave function within mean-field theory, the BMF wave function, and (ii) the Gross-Pitaevskii solution. We found that the GP wave function is identical to the BMF solution up to some barrier height. However, once the true many-body solution starts to fragment the BMF wave function is no longer given by a GP type permanent  $|N, 0\rangle$ , but rather by a fragmented state of the form  $|N/2, N/2\rangle$ . In the true many-body regime neither the GP, nor the BMF solution provide an adequate approximation to the many-body wave function, and the predicted correlations are inaccurate.

While the GP mean-field is only accurate at low barrier heights, the BMF solution provides a very good approximation to the true many-body wave function at low *and* high

barriers. We have shown that the GP mean-field predicts qualitatively wrong results at high barriers. The BMF only fails at intermediate barrier heights where the true many-body wave function becomes a superposition of many permanents. Such many-body effects can, by construction, not be captured by mean-field methods.

In the mean-field regimes at high and low barriers we have provided an analytical mean-field model that allows us to understand the general structure of the computed correlation functions.

Our work sheds new light on the first- and second-order correlation functions of interacting many-body systems. The variation of the shape of the trapping potential allows one to change the physics of the system from mean-field to strongly correlated many-body physics. Particularly, the many-body regime in between the condensed and the fully fragmented regimes has shown to be very rich and promises exciting results for experiments to come.

## ACKNOWLEDGMENTS

Financial support by the DIP - Deutsch-Israelische Projektkooperation and the DFG - Deutsche Forschungsgemeinschaft is gratefully acknowledged.

## APPENDIX A: $p$ -PARTICLE MOMENTUM DISTRIBUTION

The relation of the  $p$ -particle momentum distribution to the  $p$ -th order RDM is shown. The  $p$ -particle RDM is related to the  $p$ -particle momentum distribution by

$$\rho^{(p)}(\mathbf{k}_1, \dots, \mathbf{k}_p | \mathbf{k}_1, \dots, \mathbf{k}_p; t) = \frac{1}{(2\pi)^{Dp}} \int d^p \mathbf{r} d^p \mathbf{r}' e^{-i \sum_{l=1}^p \mathbf{k}_l (\mathbf{r}_l - \mathbf{r}'_l)} \rho^{(p)}(\mathbf{r}_1, \dots, \mathbf{r}_p | \mathbf{r}'_1, \dots, \mathbf{r}'_p; t). \quad (\text{A1})$$

The change of variables  $\mathbf{R}_i = \frac{\mathbf{r}_i + \mathbf{r}'_i}{2}$ ,  $\mathbf{s}_i = \mathbf{r}_i - \mathbf{r}'_i$  for  $i = 1, \dots, p$  in Eq. (A1) leads to

$$\rho^{(p)}(\mathbf{k}_1, \dots, \mathbf{k}_p | \mathbf{k}_1, \dots, \mathbf{k}_p; t) = \int d^p \mathbf{s} e^{-i \sum_{l=1}^p \mathbf{k}_l \mathbf{s}_l} \gamma^{(p)}(\mathbf{s}_1, \dots, \mathbf{s}_p; t), \quad (\text{A2})$$

where

$$\gamma^{(p)}(\mathbf{s}_1, \dots, \mathbf{s}_p; t) = \int d^p \mathbf{R} \rho^{(p)}(\mathbf{R}_1 + \frac{\mathbf{s}_1}{2}, \dots, \mathbf{R}_p + \frac{\mathbf{s}_p}{2} | \mathbf{R}_1 - \frac{\mathbf{s}_1}{2}, \dots, \mathbf{R}_p - \frac{\mathbf{s}_p}{2}; t) \quad (\text{A3})$$

is the average of the value of  $\rho^{(p)}(\mathbf{r}_1, \dots, \mathbf{r}_p | \mathbf{r}'_1, \dots, \mathbf{r}'_p; t)$  at distances  $\mathbf{s}_i$  between  $\mathbf{r}_i$  and  $\mathbf{r}'_i$ . From Eqs. (A2-A3) it is clear that the  $p$ -particle momentum distribution at large momenta

is determined by the behavior of  $\rho^{(p)}(\mathbf{r}_1, \dots, \mathbf{r}_p | \mathbf{r}'_1, \dots, \mathbf{r}'_p; t)$  at short distances, whereas at low momenta the off-diagonal long range behavior of  $\rho^{(p)}(\mathbf{r}_1, \dots, \mathbf{r}_p | \mathbf{r}'_1, \dots, \mathbf{r}'_p; t)$  contributes the major part.

- 
- [1] M. H. Anderson, J. R. Ensher, M. R. Matthews, C. E. Wieman, and E. A. Cornell, *Science* **269**, 198 (1995).
  - [2] C. C. Bradley, C. A. Sackett, J. J. Tollett, and R. G. Hulet, *Phys. Rev. Lett.* **75**, 1687 (1995).
  - [3] K. B. Davis, M.-O. Mewes, M. R. Andrews, N. J. van Druten, D. S. Durfee, D. M. Kurn, and W. Ketterle, *Phys. Rev. Lett.* **75**, 3969 (1995).
  - [4] E. A. Burt, R. W. Ghrist, C. J. Myatt, M. J. Holland, E. A. Cornell, and C. E. Wieman, *Phys. Rev. Lett.* **79**, 337 (1997).
  - [5] L. Cacciapuoti, D. Hellweg, M. Kottke, T. Schulte, W. Ertmer, J. J. Arlt, K. Sengstock, L. Santos, and M. Lewenstein, *Phys. Rev. A* **68**, 053612 (2003).
  - [6] B. L. Tolra, K. M. O'Hara, J. H. Huckans, W. D. Phillips, S. L. Rolston, and J. V. Porto, *Phys. Rev. Lett.* **92**, 190401 (2004).
  - [7] S. Fölling, F. Gerbier, A. Widera, O. Mandel, T. Gericke and I. Bloch, *Nature* **434**, 481 (2005).
  - [8] M. Schellekens, R. Hoppeler, A. Perrin, J. V. Gomes, D. Boiron, A. Aspect, and C. I. Westbrook, *Science* **310**, 648 (2005).
  - [9] A. Öttl, S. Ritter, M. Köhl, and T. Esslinger, *Phys. Rev. Lett.* **95**, 090404 (2005).
  - [10] L. E. Sadler, J. M. Higbie, S. R. Leslie, M. Vengalattore, and D. M. Stamper-Kurn, *Phys. Rev. Lett.* **98**, 110401 (2007).
  - [11] S. Ritter, A. Öttl, T. Donner, T. Bourdel, M. Köhl, and T. Esslinger, *Phys. Rev. Lett.* **98**, 090402 (2007).
  - [12] M. Naraschewski and R. J. Glauber, *Phys. Rev. A* **59**, 4595 (1999).
  - [13] J. V. Gomes, A. Perrin, M. Schellekens, D. Boiron, C. I. Westbrook, and M. Belsley, *Phys. Rev. A* **74**, 053607 (2006).
  - [14] M. Holzmann and Y. Castin, *Eur. Phys. J. D* **7**, 425 (1999).
  - [15] K. V. Kheruntsyan, D. M. Gangardt, P. D. Drummond, and G. V. Shlyapnikov, *Phys. Rev. Lett.* **91**, 040403 (2003).



- [16] G. E. Astrakharchik and S. Giorgini, Phys. Rev. A **68**, 031602 (2003).
- [17] R. Bach and K. Rzażewski, Phys. Rev. A **70**, 063622 (2004).
- [18] R. Pezer and H. Buljan, Phys. Rev. Lett. **98**, 240403 (2007).
- [19] S. Zöllner, H.-D. Meyer, and P. Schmelcher, Phys. Rev. A **74**, 053612 (2006).
- [20] S. Zöllner, H.-D. Meyer, and P. Schmelcher, Phys. Rev. A **74**, 063611 (2006).
- [21] S. Zöllner, H.-D. Meyer, and P. Schmelcher, Phys. Rev. Lett. **100**, 040401 (2008).
- [22] O. Penrose and L. Onsager, Phys. Rev. **104**, 576 (1956).
- [23] P. Nozières, D. Saint James, J. Phys. (Paris) **43**, 1133 (1982); P. Nozières, in *Bose-Einstein Condensation*, edited by A. Griffin, D. W. Snoke, and S. Stringari (Cambridge University Press, Cambridge, England, 1996).
- [24] R. W. Spekkens and J. E. Sipe, Phys. Rev. A **59**, 3868 (1999).
- [25] L. S. Cederbaum and A. I. Streltsov, Phys. Lett. A **318**, 564 (2003).
- [26] A. I. Streltsov, L. S. Cederbaum, and N. Moiseyev, Phys. Rev. A **70**, 053607 (2004).
- [27] O. E. Alon and L. S. Cederbaum, Phys. Rev. Lett. **95**, 140402 (2005).
- [28] O. E. Alon, A. I. Streltsov, and L. S. Cederbaum, Phys. Lett. A **347**, 88 (2005).
- [29] A. I. Streltsov, O. E. Alon, and L. S. Cederbaum, Phys. Rev. A **73**, 063626 (2006).
- [30] A. I. Streltsov, O. E. Alon, and L. S. Cederbaum, Phys. Rev. Lett. **99**, 030402 (2007).
- [31] O. E. Alon, A. I. Streltsov, and L. S. Cederbaum, J. Chem. Phys. **127**, 154103 (2007).
- [32] O. E. Alon, A. I. Streltsov, and L. S. Cederbaum, cond-mat/0703237, PRA in press.
- [33] O. E. Alon, A. I. Streltsov, and L. S. Cederbaum, Phys. Rev. Lett. **95**, 030405 (2005).
- [34] A. J. Coleman, V. I. Yukalov, *Reduced Density Matrices: Coulson's Challenge* (Springer, Berlin, 2000).
- [35] D. A. Mazziotti, Ed., *Reduced-Density-Matrix Mechanics: With Application to Many-Electron Atoms and Molecules* (Advances in Chemical Physics), Vol. 134 (Wiley, New York, 2007).
- [36] C. N. Yang, Rev. Mod. Phys. **34**, 694 (1962).
- [37] F. Sasaki, Phys. Rev. **138**, B1338 (1965).
- [38] R. J. Glauber, Phys. Rev. **130**, 2529 (1963).
- [39] U. M. Titulaer and R. J. Glauber, Phys. Rev. **140**, B676 (1965).
- [40] I. Bloch, T. W. Hänsch, and T. Esslinger, Nature **403**, 166 (2000).
- [41] H. Xiong, S. Liu, and M. Zhan, New J. Phys. **8**, 245 (2006).
- [42] L. S. Cederbaum, A. I. Streltsov, Y. B. Band, and O. E. Alon, cond-mat/0607556.

- [43] L. S. Cederbaum, A. I. Streltsov, Y. B. Band, and O. E. Alon, Phys. Rev. Lett. **98**, 110405 (2007).
- [44] M. Girardeau, J. Math. Phys. **1**, 516 (1960).
- [45] E. H. Lieb and W. Liniger, Phys. Rev. **130**, 1605 (1963).
- [46] J. B. McGuire, J. Math. Phys. **5**, 622 (1964).
- [47] M. D. Girardeau and E. M. Wright, Phys. Rev. Lett. **84**, 5691 (2000).
- [48] V. I. Yukalov and M. D. Girardeau, Laser Phys. Lett. **2**, 375 (2005).
- [49] K. Sakmann, A. I. Streltsov, O. E. Alon, and L. S. Cederbaum, Phys. Rev. A **72**, 033613 (2005).
- [50] M. D. Girardeau, Phys. Rev. Lett. **97**, 100402 (2006).
- [51] A. G. Sykes, P. D. Drummond, and M. J. Davis, Phys. Rev. A **76**, 063620 (2007).
- [52] H. Buljan, R. Pezer, and T. Gasenzer, arXiv:0709.1444, PRL in press.
- [53] E. P. Gross, Nuovo Cimento **20**, 454 (1961).
- [54] L. P. Pitaevskii, Zh. Eksp. Teor. Fiz. **40**, 646 (1961); Sov. Phys. JETP **13**, 451 (1961).
- [55] C. J. Pethick and H. Smith, *Bose-Einstein Condensation in Dilute Gases* (Cambridge University Press, Cambridge, England, 2002).
- [56] L. Pitaevskii and S. Stringari, Phys. Rev. Lett. **83**, 4237 (1999).
- [57] A. Perrin, H. Chang, V. Krachmalnicoff, M. Schellekens, D. Boiron, A. Aspect, and C. I. Westbrook, Phys. Rev. Lett. **99**, 150405 (2007).

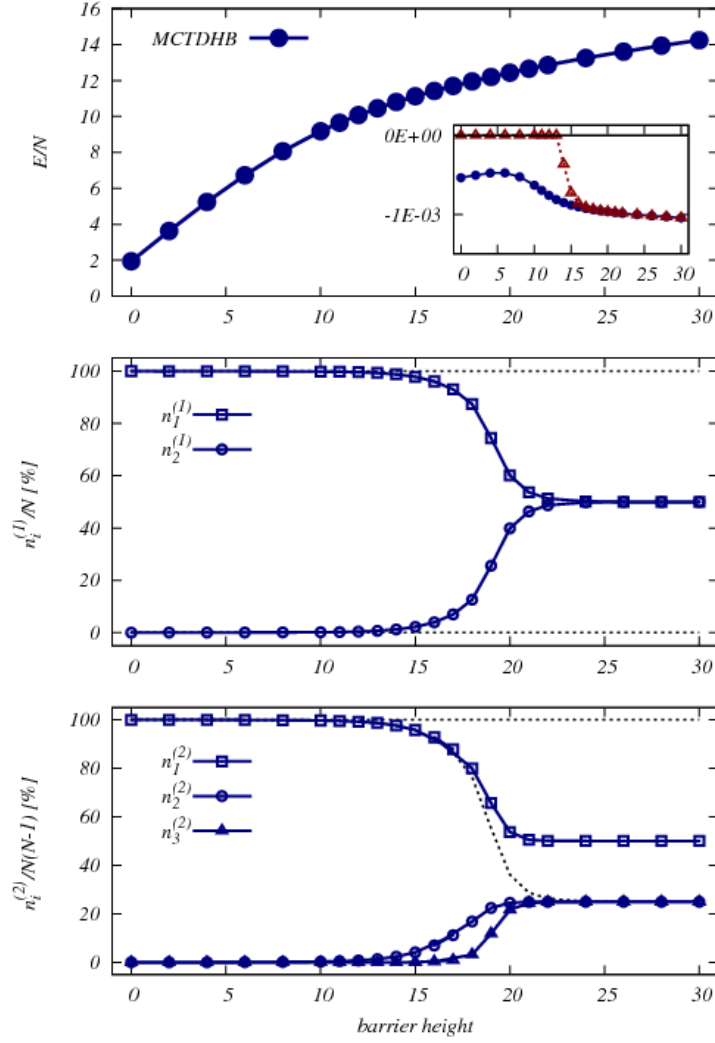


FIG. 1: (color online). Energy per particle, natural orbital and natural geminal occupations of the ground state of  $N = 1000$  bosons at  $\lambda_0 = 0.01$  in a harmonic trap with a central barrier. Shown is the dependence on the barrier height. Top: energy per particle  $E/N$  of the many-body solution. Inset: energy difference per particle between the best mean-field and the GP solution,  $(E_{BMF} - E_{GP})/N$  (triangles), and between the many-body and GP solution,  $(E_{MCTDHB} - E_{GP})/N$  (circles). Middle: the eigenvalues  $n_1^{(1)}$  and  $n_2^{(1)}$  of the first-order RDM  $\rho^{(1)}(x_1|x'_1)$ . The ground state fragments with increasing barrier height. Bottom: the eigenvalues  $n_1^{(2)}$ ,  $n_2^{(2)}$  and  $n_3^{(2)}$  of the second-order RDM  $\rho^{(2)}(x_1, x_2|x'_1, x'_2)$ . The dashed lines in the middle and bottom panel indicate upper and lower bounds on the largest eigenvalue of the first- and second-order RDMs. See text for details. The quantities shown are dimensionless.

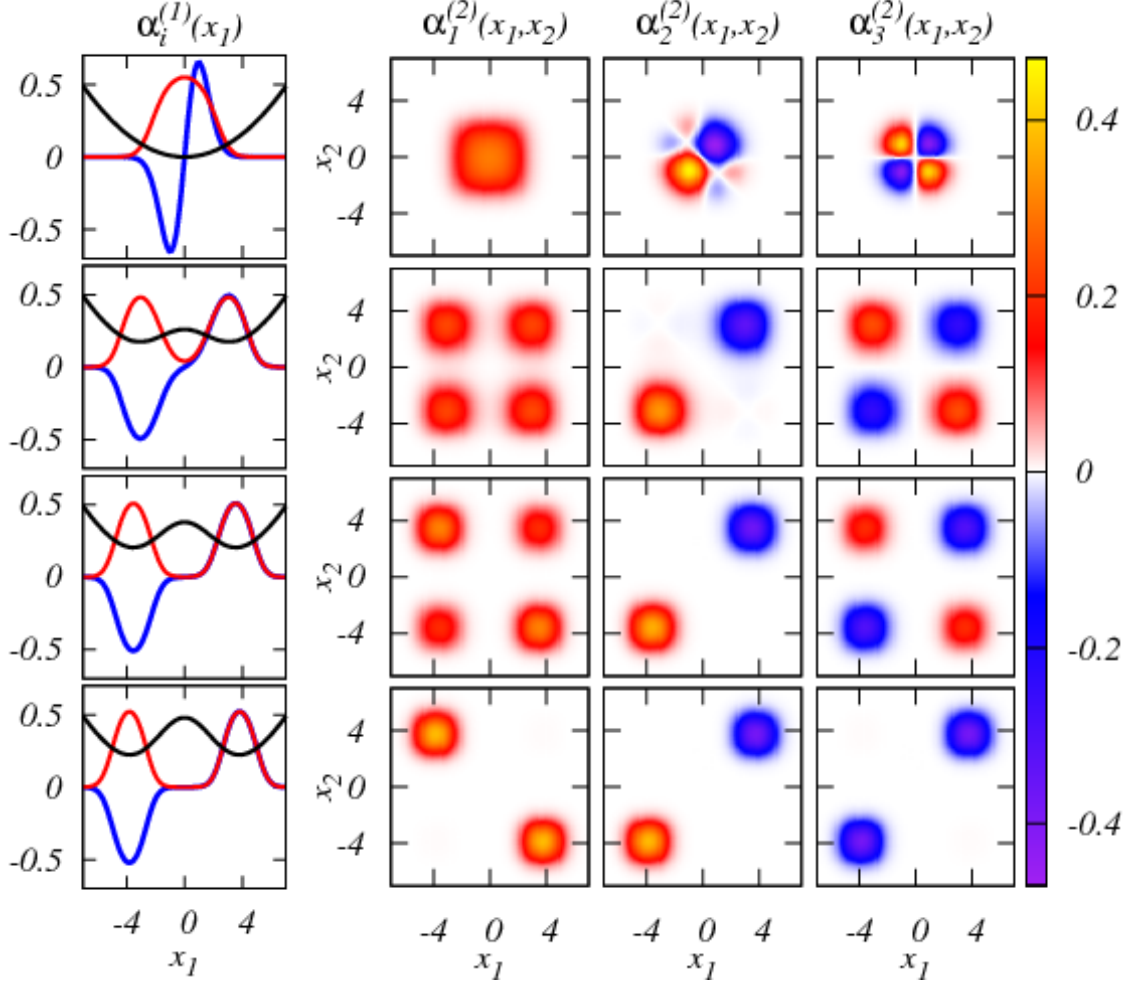


FIG. 2: (color online). Natural orbitals and geminals at different barrier heights. First column: the natural orbitals  $\alpha_1^{(1)}(x_1)$  (red line) and  $\alpha_2^{(1)}(x_1)$  (blue line) of the many-body solution at different barrier heights  $A = 0, 13, 19, 24$ , from top to bottom. The trapping potential is shown as a black line in the first column. The state of the system changes from condensed to fragmented between  $A = 13$  and  $A = 24$ . Second to fourth columns: natural geminals  $\alpha_1^{(2)}(x_1, x_2)$ ,  $\alpha_2^{(2)}(x_1, x_2)$  and  $\alpha_3^{(2)}(x_1, x_2)$  from left to right at the same barrier heights as above. While the natural orbitals remain qualitatively unchanged during the fragmentation transition, the natural geminals take on their final shapes only when the system becomes fully fragmented. At low barrier heights only one natural geminal is occupied. At high barriers three natural geminals are occupied, see Fig. 1. The total energy is minimized by the occupation of a natural geminal that contributes practically nothing to the interaction energy. See text for more details. The quantities shown are dimensionless.

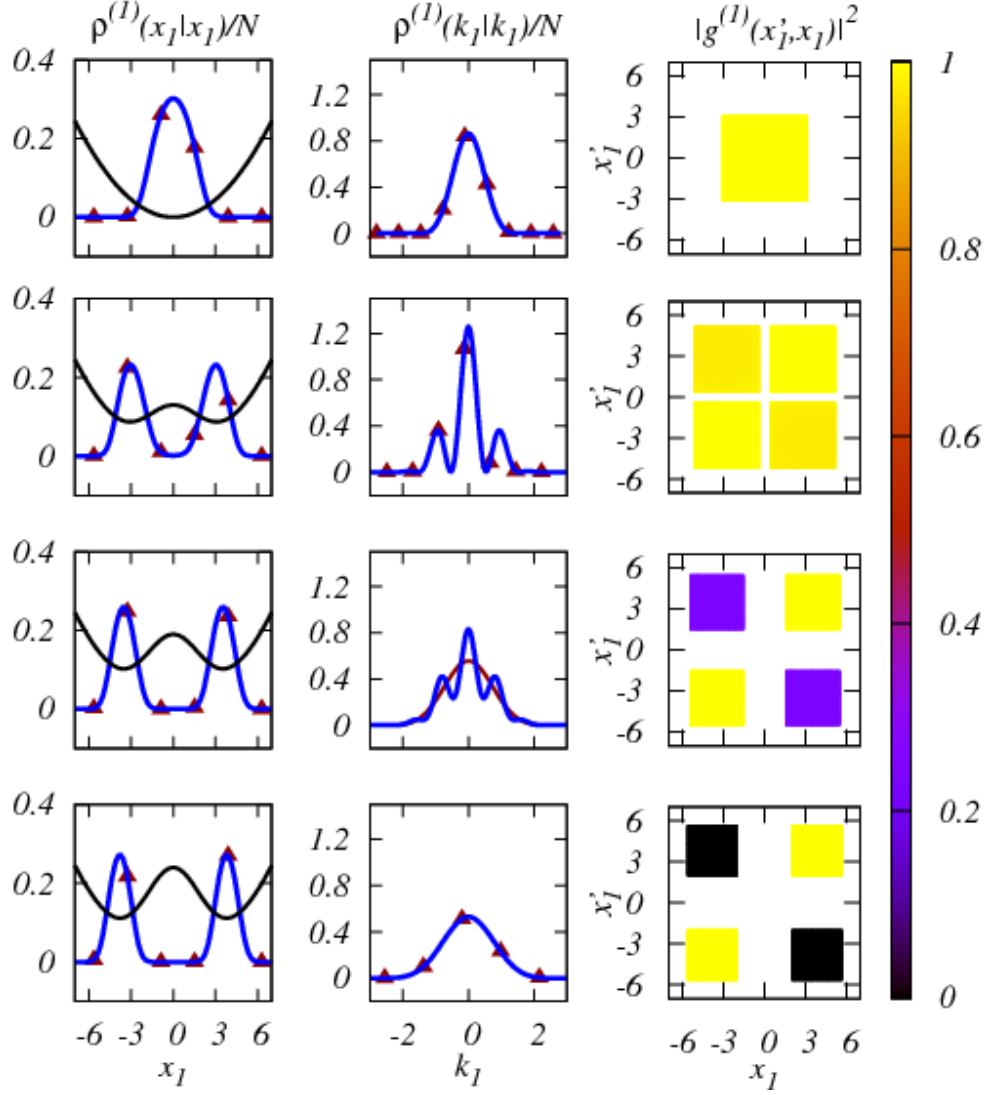


FIG. 3: (color online). Density distribution, momentum distribution and first-order coherence. The first two columns show the one-particle density  $\rho^{(1)}(x_I|x_I)/N$  and the one-particle momentum distribution  $\rho^{(1)}(k_I|k_I)/N$  of the many-body solution (blue line) and of the BMF solution (red line with triangles), respectively. From top to bottom the height of the central barrier is  $A = 0, 13, 19, 24$ . The BMF result agrees well with the many-body result for a large range of barrier heights. At  $A = 19$ , in the many-body regime, deviations are visible in the momentum distribution. See text for details. The third column shows the absolute value squared of the normalized first-order correlation function  $|g^{(1)}(x'_I, x_I)|^2$  at the same barrier heights. An initially coherent condensate splits into two separate condensates which are no longer mutually coherent. Only the coherence within each of the wells is preserved. The quantities shown are dimensionless.

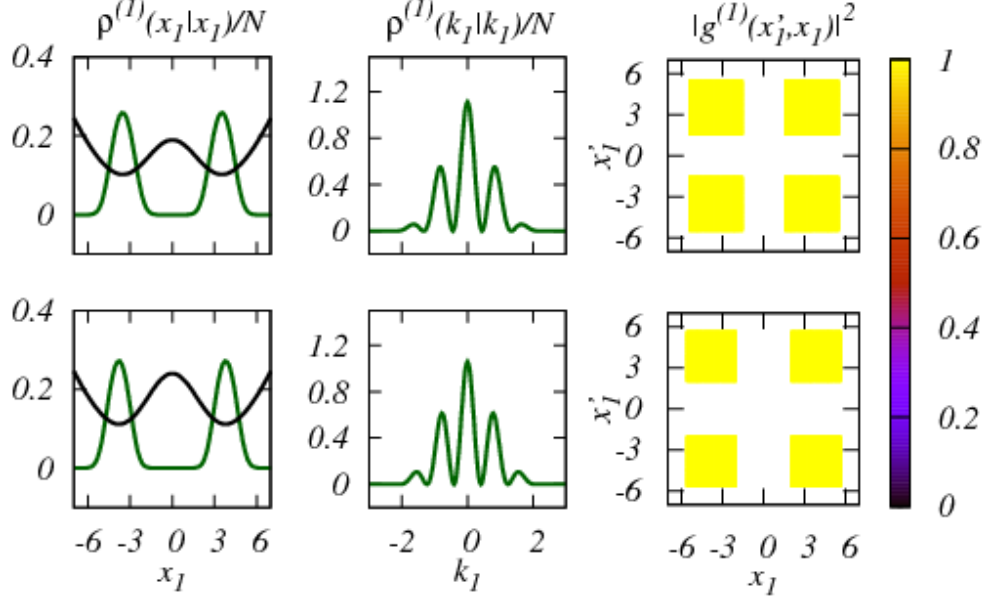


FIG. 4: (color online). Density distribution, momentum distribution and first-order coherence obtained by using the GP equation for high barriers. The first two columns show the GP one-particle density  $\rho^{(1)}(x_1|x_1)/N$  (left) and the GP one-particle momentum distribution  $\rho^{(1)}(k_1|k_1)/N$  (middle) at barrier heights  $A = 19$  and  $A = 24$  (solid green lines). In the first column the trapping potential is also shown (solid black line). The GP equation models the density well, but fails at the computation of the momentum distribution, compare with Fig. 3. The third column shows the absolute value squared of the normalized first-order correlation function  $|g^{(1)}(x'_1, x_1)|^2$  computed with the GP equation at the same barrier heights. The normalized first-order correlation function is incorrectly described by the solution of the GP equation. The quantities shown are dimensionless.

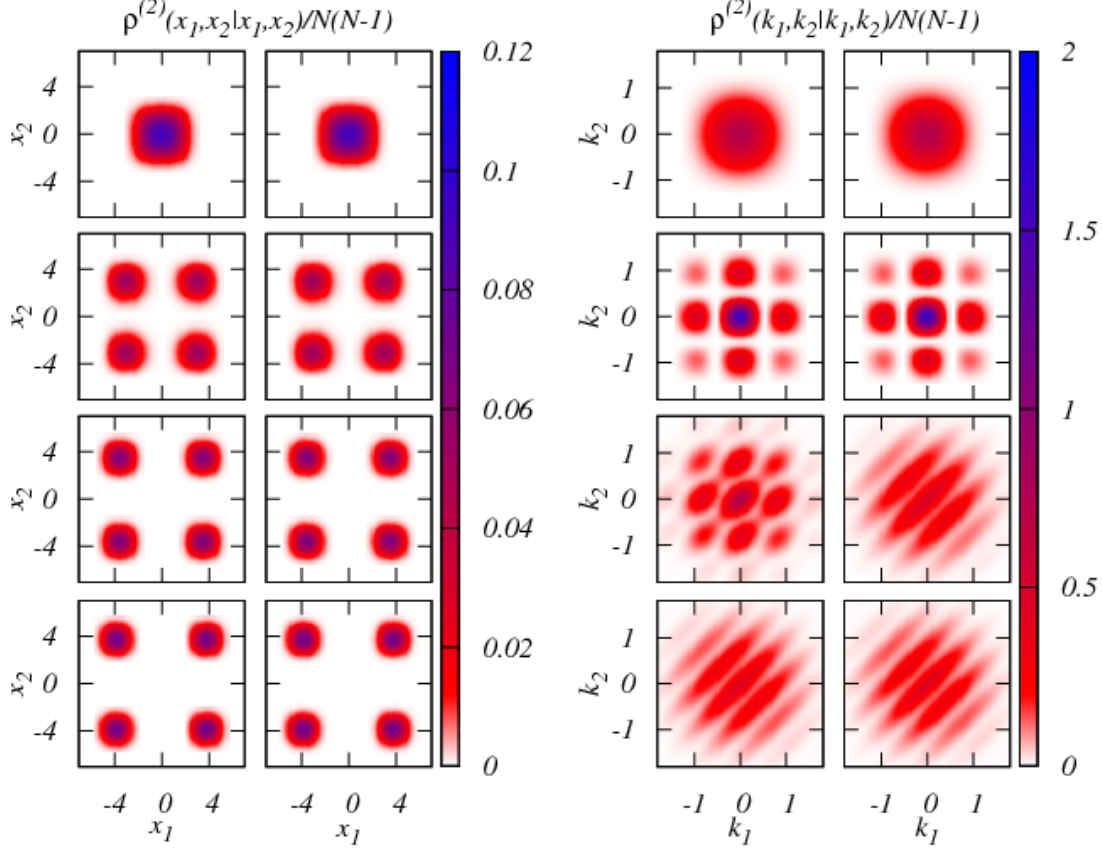


FIG. 5: (color online). Two-particle density and two-particle momentum distribution at different barrier heights. The first two columns (from left to right) show the two-particle density  $\rho^{(2)}(x_1, x_2 | x_1, x_2) / N(N-1)$  of the many-body (left) and BMF (right) wave function for the barrier heights  $A = 0, 13, 19, 24$ , from top to bottom. At low barrier heights ( $A = 0, 13$ ) the system is condensed, and the two-particle RDM factorizes into a product of the one-particle RDMs. At higher barriers ( $A = 19, 24$ ), the system fragments and the two-particle RDM does not factorize into a product of the one-particle RDMs. The two-particle density at high barriers looks very similar to that of the condensed state at  $A = 13$ . The fragmentation transition is not visible in the two-particle density. The results of the many-body and BMF wave function cannot be distinguished at any barrier height. The third and fourth column show the two-particle momentum distribution  $\rho^{(2)}(k_1, k_2 | k_1, k_2) / N(N-1)$  of the many-body (left) and BMF (right) solution at the same barrier heights as above. The transition from a condensed state to a fragmented state is clearly visible. At  $A = 19$  the BMF solution does not reproduce the many-body results. The system is in a true many-body state, inaccessible to mean-field methods. At even higher barriers  $A \geq 24$  the system fully fragments, and a mean-field description is applicable again. The quantities shown are dimensionless.

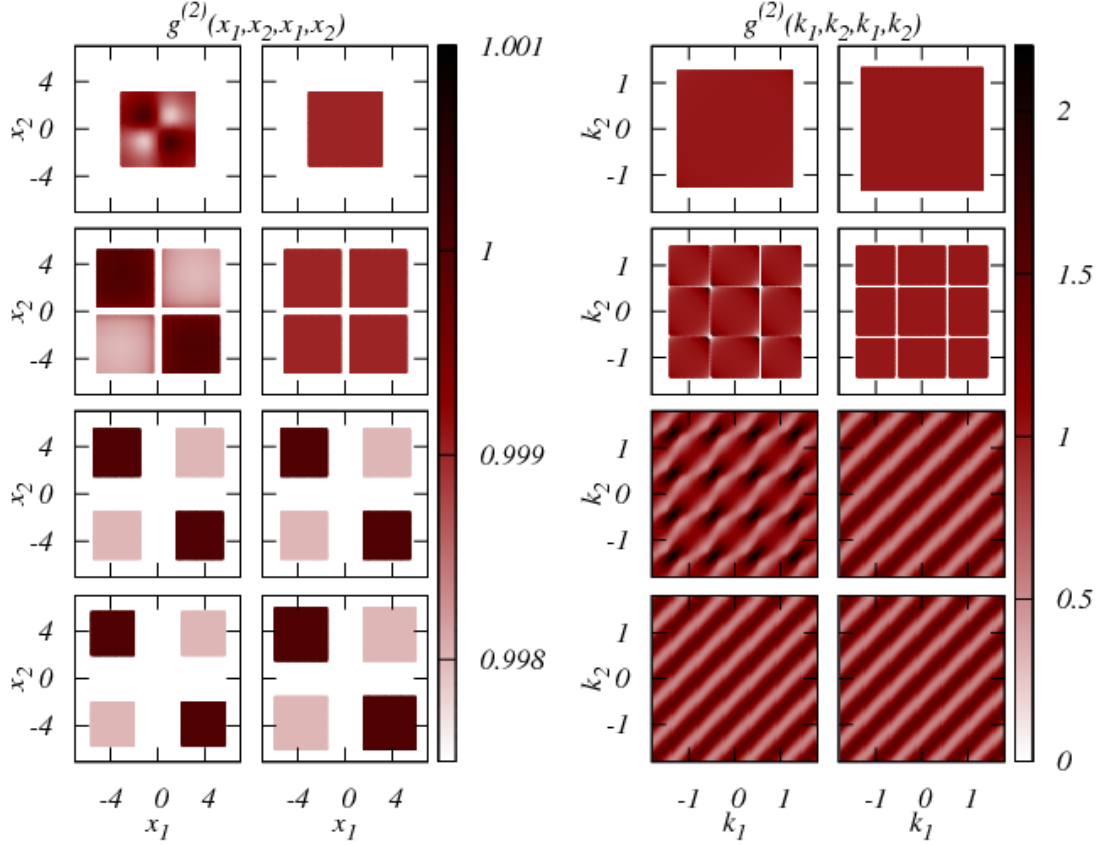


FIG. 6: (color online). Second order coherence at different barrier heights. The first two columns (from left to right) show the diagonal of the normalized second-order correlation function in real space  $g^{(2)}(x_1, x_2, x_1, x_2)$  of the many-body (left) and BMF (right) solution at barrier heights  $A = 0, 13, 19, 24$ , from top to bottom.  $g^{(2)}(x_1, x_2, x_1, x_2)$  is very close to one at all barrier heights. Note the scale! The system seems to be second-order coherent and the results of the many-body and BMF solution agree well with each other. The third and fourth column depict the diagonal of the normalized second-order correlation function in momentum space  $g^{(2)}(k_1, k_2, k_1, k_2)$  of the many-body (left) and BMF (right) solution at the same barrier heights. The fragmentation transition is clearly visible between  $A = 13$  and  $A = 24$ . At  $A = 19$  there are strong many-body correlations between the momenta (local maxima in black color) and  $g^{(2)}(k_1, k_2, k_1, k_2)$  exhibits a complicated pattern, see text for more details. A mean-field description fails here. In the limit of high barriers,  $A \geq 24$ , the correlations of the many-body state become again describable by those of the BMF solution. The quantities shown are dimensionless.